Modelling the time-dependent mechanical behaviour of clay rocks based on meso- and micro-structural viscous properties

Sun, Yufeng; Pardoen, Benoît; van den Eijnden, Bram; Wong, Henry

DOI
10.1002/nag.3617

Publication date
2023

Document Version
Final published version

Published in
International Journal for Numerical and Analytical Methods in Geomechanics

Citation (APA)
Sun, Y., Pardoen, B., van den Eijnden, B., & Wong, H. (2023). Modelling the time-dependent mechanical behaviour of clay rocks based on meso- and micro-structural viscous properties. *International Journal for Numerical and Analytical Methods in Geomechanics*, *47*(17), 3177-3208. https://doi.org/10.1002/nag.3617

Received: 25 March 2023 | Revised: 16 August 2023 | Accepted: 21 August 2023

DOI: 10.1002/nag.3617

RESEARCH ARTICLE

WILEY

Modelling the time-dependent mechanical behaviour of clay rocks based on meso- and micro-structural viscous properties

Yufeng Sun[1] | **Benoît Pardoen**[1] | **Bram van den Eijnden**[2] | **Henry Wong**[1]

[1]LTDS, University of Lyon, ENTPE, Lyon, France

[2]Department of Geoscience and Engineering, Delft University of Technology, Delft, Netherlands

Correspondence
Yufeng Sun, LTDS, University of Lyon, ENTPE, Lyon, France.
Email: yufeng.sun@entpe.fr

Funding information
China Scholarship Council, Grant/Award Numbers: File No., 202006560007

Abstract

Clay rocks are multiphase porous media having a complex structure and behaviour characterised by heterogeneity, damage and viscosity, existing on a wide range of scales. The mesoscopic scale of mineral inclusions embedded in a clay matrix has an important role in the mechanisms of deformation under mechanical loading by cracking and creeping. This study introduces a micromechanical approach to model the time-dependent mechanical behaviour of clay rocks. A heterogeneous clay rock is represented at the mesoscopic scale as a composite material consisting of rigid elastic mineral inclusions (quartz, calcite and pyrite) embedded in a clay matrix. To describe the damageable rock behaviour and its failure modes at the small scale, interfaces between different mineral phases and within the clay matrix are considered. Viscous effects are incorporated inside the clay aggregates, with intergranular microfractures propagating in the clay matrix, in order to investigate their contribution to the creep behaviour of clay rock at the macroscale. The mesostructure of the clay rock is represented in digital 2D Representative Elementary Areas (REAs). The overall mesoscale behaviour of the clay rock under mechanical solicitation is numerically obtained from the REA by computational homogenisation within a two-scale finite element squared framework. Then, the model is validated at mesoscale against experimental data. The variability of the material response and the time evolution of the mineral interfacial damage state are investigated in relation to the small-scale properties and failure, while considering mesostructure variability. The results can give some valuable insights into creep behaviour of the clay rock from a small-scale perspective.

KEYWORDS
clay rock, creep, microstructural variability, multiscale numerical model, viscosity

1 | INTRODUCTION

In the context of the deep geological repository of high-level radioactive wastes, clays and clay rocks are being investigated as the potential host rock due to their low permeability and (re)sealing capacity in several countries.[1–3] For example, the Callovo-Oxfordian (COx) claystone in France, the Opalinus clay in Switzerland, and the Boom clay in Belgium.[4] These clay rocks and plastic clay have complex mineral compositions and multi-scale structures, from the microscopic scale of clay platelets and aggregates, to the mesoscopic scale of mineral arrangement, then to the macroscopic scale of geological heterogeneities. Hereafter, the COx claystone behaviour is studied, from micro- to meso-scale. A particular attention should be paid on the definition of the mesoscale, which refers to the scale of the heterogeneous spatial arrangement of the minerals in this paper.

At the macroscale, analyses of in situ measurements (e.g., gallery convergence, deformation, pore pressure) lead to the distinction of two major phenomena[5]: (1) plastic deformations due to damage and (2) creep. Firstly, elastoplastic and damage mechanisms seem to dominate the short-term behaviour of the COx claystone around large-scale underground galleries. During gallery excavation, irreversible plastic deformations and fracture networks appear and evolve rapidly around the galleries due to the quasi-brittle behaviour of the indurated clay rock. By contrast, during service life and more importantly during the post-closure period, deformations evolve relatively slowly. The time-dependent behaviour of the clay rock, due to the creep of the clay matrix and propagation of induced fractures, appears to be more predominant at this latter stage. Thereby, it significantly affects the design of the support system for their long-term stability. Indeed, the confining capacity of a geological barrier for radioactive wastes can be affected by the creep deformations and subcritical propagation of cracks in rocks.[6–10] Therefore, it is necessary to investigate both the short- and the long-term behaviour of the host rock around galleries to ensure safety and sustainability of the underground repository. On short term behaviour, extensive laboratory investigations have shown that the mechanical behaviour of clay rocks can be characterised by coupled plastic damage.[11] Concerning long term behaviour, time-dependent creep deformation constitutes another important feature of clay rocks.[3,12–15] Classically, the time-dependent inelastic deformation of a material is described by phenomenological viscoplastic models (e.g., Bui et al.[16]; Sun et al.[17]). Although these models provide efficient mathematical tools for the long-term analyses of structures, the physical mechanisms of creep deformation are not explicitly considered. In consequence, these models cannot account for the effects of mineral composition and geometry of microstructures on the mechanical response of argillaceous rocks. Therefore, it is necessary and useful to study the small-scale behaviour of clay rock to better explain the time-dependent mechanisms observed from small to large scales, and also to provide a better basis for further extension of macroscale constitutive models.

At the mesoscale, clay rocks are heterogeneous and composed of several types of mineral inclusions embedded in a clay matrix.[18–20] At this scale, the behaviour of rocks is characterised by the morphological (size and shape) and material properties of the components and their interactions. The mesoscopic scale has an important role in the mechanisms of deformation under mechanical loading by cracking[21] and creeping.[22] At the microscale, the clay matrix is composed of clay aggregates (made of “clusters” of clay particles, or clay platelets, in turn made of a stack of atomic layers, etc. as going downscale),[23] interacting between them and with the mineral inclusions. The influence and accurate reproduction of these micro- and meso-scale characteristics on the large-scale material behaviour, accounting for damage and viscosity, remains a complex issue. This becomes an essential concern to investigate the short- and long- term underground stability of galleries and tunnels during and after excavation process.

Considering the complex mesostructure of clay rocks, one possibility to evaluate their impacts on mesoscale and macroscale overall mechanical responses is to use a multi-scale approach. Such approach allows to study a statistically equivalent Representative Elementary Volume (REV for 3D case) or Representative Elementary Area (REA for 2D case) to determine the behaviour of the equivalent homogeneous medium.[24–33] In particular, computational homogenisation methods,[34–36] also known as multi-scale analyses, have emerged. They include, among others, finite element squared (FE^2)[24,37–40] and FEM-DEM[41] methods for continuous media at the large scale and heterogeneous/discrete material at the small scale. This approach does not introduce any explicit expression for the macroscale constitutive equations, as the homogenised response from the mesoscale computation serves as a numerical constitutive relation in the macroscale continuum. To this date, modelling of the time-dependent behaviour of clay rocks accounting for small-scale characteristics and scale transition from the mesoscale to the macroscale remain insufficiently investigated. Therefore, the main objectives of the present work are to (1) develop a multiscale creep model of clay rock, to (2) discuss the contribution of viscosity in clay aggregates and clay aggregate contacts to the overall creep behaviour of claystone from a small-scale perspective, and to (3) provide some valuable insights into the microscopic mechanisms of creep-induced damage.

The article is organised as follows: Section 2 details the structure and viscous behaviour of clay rocks. A short introduction on the mesostructure of the studied material, the COx claystone, is given with the modelling possibilities of its viscosity. Section 3 gives the modelling approach from meso- and micro-scales aspect. Section 4 introduces the framework of mesoscale model of the clay rock, for example, the periodic mesostructure and boundary conditions, the homogenisation method. The microscale constitutive models of solid minerals, their contacts (i.e., mineral interfaces), and their numerical implementations are also described. In Section 5, the ability of the proposed micro- and meso-scale models

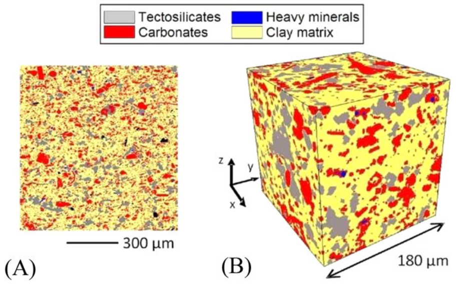

FIGURE 1 Spatial distribution of mineral groups of the COx claystone: (A) 2D SEM image on a section perpendicular to the bedding planes; (B) 3D micro-CT subvolume (EST26095).[20]

to describe the instantaneous and long-term mechanical behaviour of clay rocks is assessed by comparing numerical results with experimental data obtained from triaxial and creep compression tests. The influences of viscosity inside clay aggregates or at inter-aggregate contacts on the overall creep deformation and damage modes are investigated.

2 | CLAY ROCK STRUCTURE AND BEHAVIOUR

A description of the micro- and meso-structures of heterogeneous clay rocks and some fundamental aspects of their mechanical behaviour at different scales is given in this section. First, it is necessary to define the different scales which are considered:

- Microscopic scale (µm): scale of the mineral inclusions, clay aggregates and fracture porosity.
- Mesoscopic scale (mm): scale of the heterogeneous spatial arrangement of the minerals, thus of the mineral inclusions, of the connected clay matrix and of the interactions between the mineral components. This mesostructure is studied in a single material point in this study.
- Macroscopic scale (cm): scale of pluricentimetric laboratory samples, at which the material is modelled as a continuum.

2.1 | Micro- and meso-structures of the Callovo-Oxfordian claystone

As aforementioned, we focus hereafter on the COx claystone. This clay rock is the host rock envisaged for deep geological nuclear waste repository in France, and studied by Andra in its Underground Research Laboratory (URL) located in Bure (Meuse/Haute-Marne area) at approximately 490 m depth.[1] This argillaceous rock is mainly composed of four mineral components, as visible in Figure 1: tectosilicates ($-Si_xO_y$, mainly quartz, 10%–40%), carbonates ($-CO_3$, mainly calcite, 15%–80%), heavy minerals (FeS_2, pyrite, in a low proportion of 0%–3%) and clay minerals (mainly illite and interstratified illite/smectite, 20%–60%).[12,20] From the work of Cosenza et al.,[18,19] the average contents of these four minerals in the COx clay-rich lithostratigraphic unit are 18%, 30%, 2% and 50% based on detailed experimental investigations.

As a multiphase composite material with strong heterogeneity, this claystone has a complex (micro)structure with multiple characteristic lengths.[20] 2D and 3D spatial distributions of the mineral groups of the COx claystone obtained from the analyses of x-ray computed micro-tomography (micro-CT) and scanning electron microscopy (Backscattered Electrons, SEM BSE) images are shown in Figure 1. These analyses lead to the determination of mineral groups, spatial distributions, mineral area fractions and mineral morphology (size, shape and orientation of mineral inclusions). Therefore, the COx claystone will be considered as a solid four-phase composite material in which three different types of mineral inclusions (quartz, calcite and pyrite) are embedded in a clay matrix.

2.2 | Mechanical behaviour of the Callovo-Oxfordian claystone

2.2.1 | Macroscale behaviour

The mechanical behaviour of the COx claystone, observed from experimental observations and laboratory tests, is briefly described in the following.

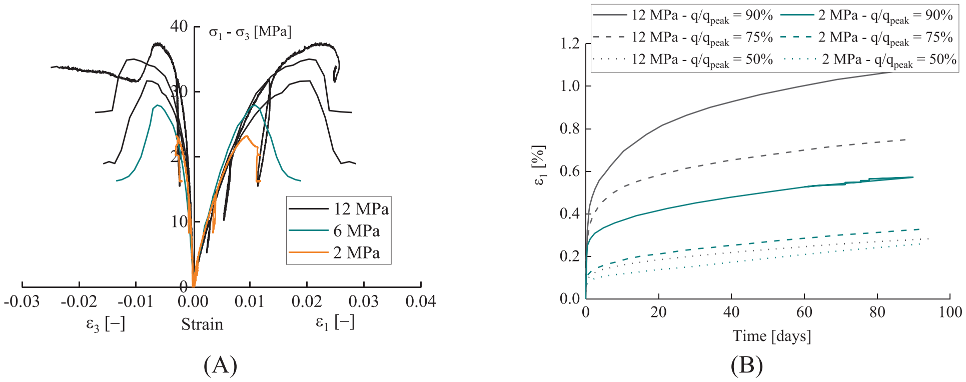

(A) (B)

FIGURE 2 Laboratory results on COx claystone with a relative humidity of 90% conducted by Armand et al.[12]: (A) triaxial compression tests and (B) triaxial creep tests under different confining pressures.

Considering the short-term behaviour, in typical loading-unloading(-reloading) cycles of deviatoric stress on samples,[42] large residual strains in both axial and lateral directions are observed after unloading the deviatoric stress. Furthermore, triaxial compression tests (as shown in Figure 2A) performed for different confining pressures[5] have shown that, like other claystones, the mechanical behaviour of COx claystone has a strong dependence on the surrounding pressure. As the mean (compressive) stress level increases, the shear strength of the argillaceous rock increases and a transition from brittle to ductile behaviour is observed. In its in situ environment and under in situ stress range, the COx claystone exhibits a quasi-brittle behaviour. The observed peak stresses in material stress-strain response curves correspond to the maximum compressive and shear strength of the rock reached under uniaxial and triaxial compression tests. At the macroscale, the peak stress corresponds to the initiation of a fracture in the rock specimen leading to its failure. Then, strain softening is observed after the peak stress where micro- and macro-cracks are generally observed in the sample after failure.[21]

Considering the long-term behaviour, creep tests (as shown in Figure 2B) under different constant confining pressures and deviatoric stresses[12,43] indicate a time-dependent behaviour of the COx claystone, with significant creep (viscous) deformation under constant mechanical loading. The level of the deviatoric loading to which the rock is subjected to has an important effect on the amplitude and time-evolution of the specimen axial strain.[3] For instance, under uniaxial creep compression tests, the creep rate varies linearly and very slowly with stress at low stresses (below 13–15 MPa). Above a certain threshold, the creep rate increases at a higher rate with stress and deviates from a linear form.[44] No creep failure (tertiary creep) took place during any of their tests performed. Up to now, only a few results have been obtained on tertiary creep for COx claystones.[22,42] The acceleration of the creep rate appears to be related to the onset and development of microcracks (i.e., mechanical damage).[22]

2.2.2 | Meso- and micro-scale behaviours

The macroscale behaviour of rocks significantly depends on their mesoscale granular structure, which in turn depends on the microscale properties of each mineral component. At the meso- and micro-scales, the deformation in clay rocks is dominated by damage, decohesion and cracking mechanisms. With a combination of scanning electron microscopy (SEM) and broad ion beam (BIB), microstructural observations on COx claystone at microscale show that the deformation mechanisms are dominantly cataclastic and that crystal plastic mechanisms are minor.[21] Potential decohesion mechanisms around mineral inclusions and cracking within the clay matrix develop in the clay rock.[21,45] The microcracking includes inter-granular microfractures propagating in the clay matrix (i.e., inter-clay aggregates) and between mineral inclusions and clay (i.e., grain/matrix joints), as well as intragranular and trans-granular (i.e., intra- and trans-crystal) microfractures propagating in non-clay minerals.[21] The microcracking is more prone to develop along the contacts (interfaces) between non-clay minerals and clay matrix. The microcracks within the clay matrix and the decohesion around the inclusions take their origin from heterogeneities at the scale of mineral inclusions.

Furthermore, viscoplastic deformations develop in clay rocks. Plasticity and creep deformation are generally assumed to mainly occur within the clay matrix.[7,11] In fact, clay behaviour under solicitation is usually dominated by irreversible strain and the physical mechanisms of short-term plastic and time-dependant viscous deformations may be due to smaller

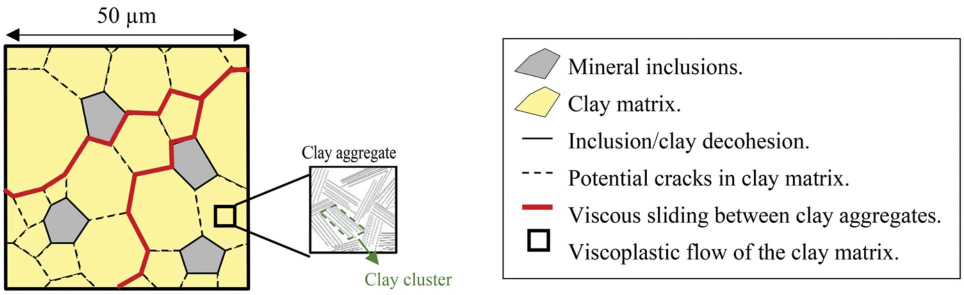

FIGURE 3 Schematic representation of the mesoscopic structure of the COx claystone with microstructural rupture modes and viscoplastic deformation.

scale heterogeneities in the clay mineral. At small scale inside the microscale clay particles, the main inelastic deformation mechanism takes place as plastic sliding of clay sheets (unit layers of clay minerals), along parallel inter-layers.[11,46] Moreover, the physical mechanism of creep deformation in clay rocks mainly includes two phenomena: the viscosity of the clay matrix (from smaller scale clay heterogeneities) and the subcritical propagation of microcracks inside the clay matrix.[6,47]

3 | MODELLING APPROACH

Following the above observations, clay rocks are considered as a heterogeneous assembly of constituents (as heterogeneous polycrystalline rocks) at the mesoscale with plasticity and viscosity considered in the clay matrix. The numerical simulations are conducted under pure mechanical condition, the influence of pore water is therefore not considered in this study, but is already part of the multiscale modelling framework (van den Eijnden et al.[37]). A schematic representation of the mesoscopic structure of the COx claystone is illustrated in Figure 3 with: the mineral inclusions embedded in the mesoscopic clay matrix, the microstructural rupture modes and the viscoplastic deformation. The microstructural rupture modes are modelled by decohesion of interfaces around the mineral inclusions and crack mechanisms within the clay matrix.[48,49] The crystal plasticity and microfractures inside the mineral inclusions (e.g., non-clay mineral grain breakage) are not represented in the model. The irreversible plastic and creep behaviour of the COx claystone is considered by introducing viscoplastic deformation of the clay matrix. The short-term plastic deformation is considered inside the clay matrix by assuming that the clay aggregates deform due to small scale processes (e.g., between clay layers inside clay particles). The time-dependent viscous deformation is considered by assuming two possible scales of viscosity: either at the mesoscopic scale of the clay matrix or at the microscopic scale of the clay aggregates (corresponding to smaller scale deformations in clay aggregates, particles, platelets, etc.). The viscosity is then introduced by the development of two viscous mechanisms schematically represented in Figure 3. Firstly, the "diffused" viscoplastic flow of the clay matrix is considered. This intra- aggregate viscoplastic flow is assumed to be due to smaller scale heterogeneities as clay particles, platelets and layers. Secondly, a viscous sliding between large clay aggregates is considered. This inter-clay aggregate viscous sliding is assumed to develop as microcracks propagate through the clay matrix.

The morphologically representative element areas (REAs) are modelled to obtain an accurate reproduction of the material structure and behaviour. An algorithm, based on Voronoï tessellation from the work of Pardoen et al.[48] and van den Eijnden et al.[49] is adopted to generate periodic 2D REAs with random microstructures. Several control parameters are added to the tessellation algorithm to be able to control the grain geometry statistics. These parameters can be used to accurately match the geometrical characteristics of the mineral inclusions geometry of COx claystone as characterised by Robinet et al.[20]

Figure 4 shows the comparison between material structure obtained from a polished thin section in a plane perpendicular to the stratigraphic plane and numerical simulation at mesoscale. The algorithm allows to generate several REAs with a certain variability of the mesostructure, for instance, with a variability of its heterogeneity (spatial variability of the mineral inclusion positions) or of its mineral content. The anisotropic behaviour at the macroscale arises naturally from the morphology of the microstructure taken at the microscale inside an REA in this construction.[49]

As for the REA size, the characteristic length of the mesostructure is $L_{REA} \approx 100$ μm defined experimentally.[18–20] Note that, if from a morphological point of view, the chosen size of the REAs is considered sufficient, this is not quite the case

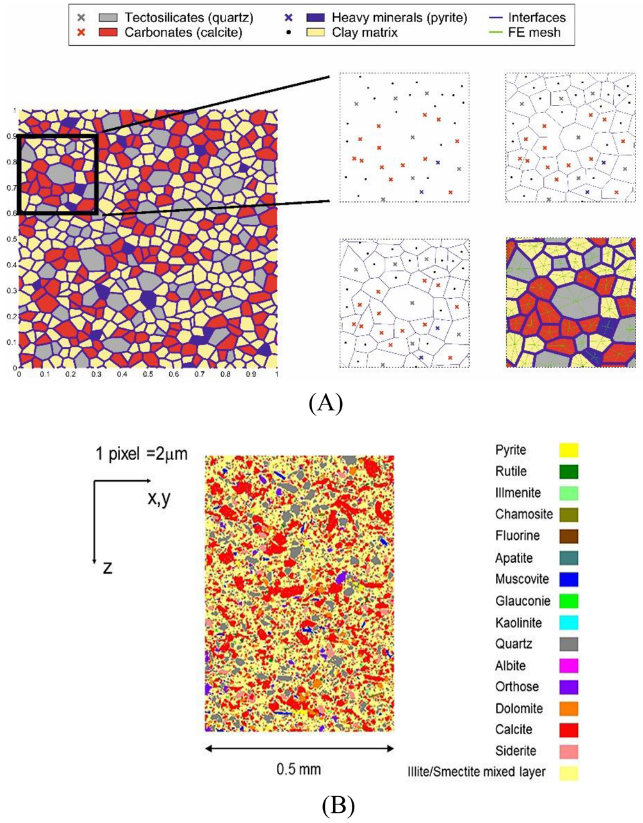

(A)

(B)

FIGURE 4 Comparison of COx structure at mesoscale obtained respectively from (A) numerical simulation (taken from Pardoen et al.[48]) and (B) a polished thin section in a plane perpendicular to the stratigraphic plane (taken from Cosenza et al.[18]).

from the point of view of the homogenised mechanical response. As for the mineral inclusions size, an artificial size is assigned to the mineral grains by considering the mean area of quartz and carbonate inclusions measured experimentally. For each type of mineral, Pardoen et al.[48] give a good agreement between the numerical and experimental results: the minimal-mean-maximal sizes are: 6—72—230 μm^2 for quartz, 6—43—115 μm^2 for carbonates and 6—35—84 μm^2 for pyrite.

The 2D elementary areas that are considered are representative of (vertical) planes normal to the (horizontal) bedding planes. This would have an influence on the failure and micro-cracks propagation.[48] In addition, previous results have shown that the 2D model overestimates material dilatancy,[49] which is related to the displacement of the solid constituents and to the opening of interfaces between them. Since rearrangement of solid constituents is not considered in the mesoscale model, this opening at solid constituent contacts occurs regardless of the deformation state. A more accurate depiction of the material microstructure can be achieved through a 3D model. However, before going to this more realistic 3D representation, the use of 2D calculations serves as a valuable foundation, providing reference results for subsequent analyses involving 3D computations. As shown in Figure 4, the 2D microstructure is enriched by taking into account realistic properties of mineral inclusions, such as morphology, area fraction and orientation. orientation, measured experimentally in 2D material sections.

4 | FRAMEWORK OF THE MESOSCALE MODEL

The formulation of the mesoscale model and of its periodic framework is defined hereafter. This model has been developed as a part of a double-scale modelling framework, the so-called FE^2 method, which allows an upscaling of the material behaviour by computational homogenisation.[37] As mentioned previously, within the framework of computational homogenisation, a mesoscale computation is carried out on a REA of which the homogenised response is considered as the local (at a Gauss point) numerical constitutive relation at macroscale. A representative sample of the material mesostructure is represented and modelled in a REA. Different components at mesoscale are described by their individual

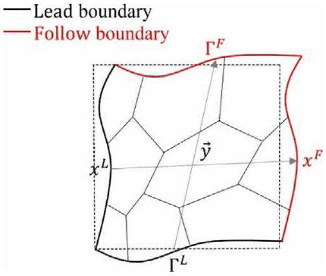

FIGURE 5 Deformed local periodic mesostructure. Homologous points x_i^F and x_i^L on periodic boundary segments Γ^F and Γ^L.

constitutive models. Considering the existence of discontinuities, as the contact interfaces between the different minerals, the small strain assumption is used at the microscale to satisfy the requirement of microscale stress continuity.

4.1 | Representative elementary area with periodic boundary conditions

The material mesostructure represented in a REA (of configurationΩ) is composed of solid particles, including elastic mineral inclusions embedded in a clay matrix, separated by cohesive interfaces. Its role is to reproduce the stress-strain behaviour of the composite material, including the non-linear behaviour which comes from the plasticity of the clay matrix, the microcracking in the clay matrix, and the decohesion at interfaces around mineral inclusions (modelled by damage and softening). Macroscale and mesoscale deformations are transferred through the periodic boundary condition of the REA.

Figure 5 shows a deformed REA with periodic boundary conditions. Due to the existence of contact interfaces with displacement discontinuities, the weak formulation requires to take into consideration both the internal interfaces Γ_{int} and the external boundary Γ. The latter is the boundary where periodic conditions are imposed and is subdivided into two parts: the "lead" part Γ^L and the "follow" part Γ^F.

The kinematics of any point x_i on the follow boundary depend on the kinematics of its corresponding homologous point on the lead boundary. The distance between these two points is defined by the period vector $\vec{y}$:

$$x_i^F = x_i^L + y_i \tag{1}$$

The mechanical part of the periodic boundary conditions of the REA is defined in terms of the mesoscale displacement u_i relationship between homologous points as:

$$u_i^F = u_i^L + \varepsilon_{ij}^M y_j \tag{2}$$

where ε_{ij}^M is the components of small strain tensor enforced on the REA. Moreover, external boundary tractions t_i need to satisfy the antiperiodic condition:

$$t_i^F + t_i^L = 0 \tag{3}$$

4.2 | Microscale constitutive model

Microscale computation allows to assign different constitutive relations to each component. Based on the microstructural observations of Section 2, an isotropic, linear and elastic behaviour is assumed for the quartz, calcite and pyrite mineral inclusions, while plasticity and viscosity are considered for the clay matrix. Moreover, the contact interfaces between solid minerals are modelled, accounting for failure and damage modes at small scale. To do so, the contact interfaces around mineral inclusions and within the clay matrix are considered as decohesive zones and potential microcracks.

For the clay matrix, an elastoplastic constitutive law is considered for the short-term behaviour whereas a viscous (elasto-viscoplastic or viscoelastic) constitutive law is considered for the long-term behaviour. For this viscous behaviour,

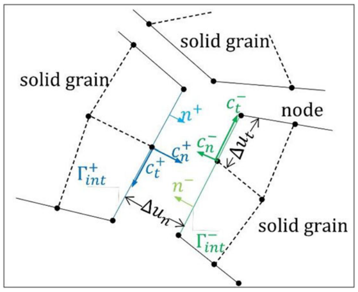

FIGURE 6 Concept of microscale mechanical modelling.

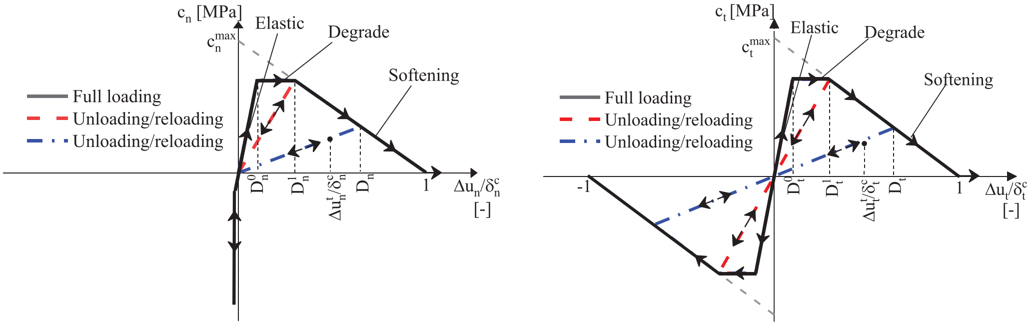

(A) (B)

FIGURE 7 Damageable cohesive interface model in the (A) normal and (B) tangential directions of contacts between mineral grains.

two microscale mechanisms have been introduced: the viscoplasticity of the clay aggregates and the viscoelasticity of their contacts.

4.2.1 | Cohesive model of mineral contacts

Figure 6 illustrates the scheme of cohesive forces acting on the internal boundaries Γ_{int}, which is subdivided into lower and upper parts $\Gamma_{int}^{-/+}$ of outward normal $n^{-/+}$. Cohesion $(c_i^{-/+}; i = t, n)$ and displacements $(u_i^{-/+} i = t, n)$ can be decomposed into normal $(i = n)$ and tangential $(i = t)$ parts, in order to account for the displacement discontinuity (i.e., interfacial opening and relative sliding) $\Delta u_i = u_i^+ - u_i^-$ across the interface. As illustrated in Figure 6, the solid phases are separated by cohesive cracks defined both in the normal and tangential directions to the mineral grain boundary. The appearance of the microcracks is due to the deformation by solid mineral grain movements (displacements) and their behaviour can be simulated by damageable cohesive interface models.

As shown in Figure 7, an interface damageable cohesive model including an elastic, a constant cohesion, a softening and a complete decohesion behavioural phases is used.[50] The model provides some flexibilities arising from the four parameters $\{D_{t/n}^0, D_{t/n}^1, \delta_{t/n}^c, c_{t/n}^{max}\}$ representing, respectively, the damage initiation, the cohesion softening initiation, the critical relative displacements for complete decohesion, and the maximum cohesive forces. For example, setting $D_{t/n}^0 = D_{t/n}^1 = 0$ leads to a linear interface cohesive model; while setting $D_{t/n}^0 = D_{t/n}^1 \neq 0$ leads to a bilinear interface cohesive model.

As indicated in Figure 7, the development of the cohesive normal and tangential forces c_n and c_t with interface opening Δu_n and sliding Δu_t (relative displacements in the normal and tangential directions) can be divided into four stages: (1) from $\frac{\Delta u_{t/n}}{\delta_{t/n}^c} = 0$ to $D_{t/n}^0$, the interface undergoes a pure elastic stage; (2) from $\frac{\Delta u_{t/n}}{\delta_{t/n}^c} = D_{t/n}^0$ to $D_{t/n}^1$, the cohesive interface starts to degrade, meanwhile, the cohesion force reaches the critical cohesive strength of the interface; (3) as the interface opening/sliding further increases beyond the point $\frac{\Delta u_{t/n}}{\delta_{t/n}^c} = D_{t/n}^1$ to 1, softening occurs and the interface cohesive force decreases continually to zero (complete decohesion); (4) when the interface opening/sliding reaches its maximum value $\frac{\Delta u_{t/n}}{\delta^c_{t/n}} = 1$, it is completely debonded and the cohesive force in the interface disappears.

The damage parameter $D_{t/n}$ represents the current interface state based on time history ($0 \leq \tau \leq t$):

$$D_{t/n} = \min\left(\max\left(D^0_{t/n}, \frac{1}{\delta^c_{t/n}} \, max_{0 \leq \tau \leq t} \left(\left| \Delta u^\tau_{t/n} \right| \right) \right), 1 \right) \tag{4}$$

If $D_{t/n} = D^0_{t/n}$, then the interface is in the elatic stage; if $D^0_{t/n} < D_{t/n} \leq D^1_{t/n}$, then the interface is in the degrade stage without softening; if $D^1_{t/n} < D_{t/n} < 1$, then the interface is in the damaged softening stage; if $D_{t/n} = 1$, then the interface is completely damaged.

Taking the normal components of interface cohesion as an example, the cohesive force c^t_n at current time t is represented mathematically as:

$$c^t_n = \left\{ \begin{array}{cc} E^0_n \, \Delta u^t_n & \Delta u^t_n \leq D^0_n \delta^c_n \\ c^{max}_n \left(1 - D^1_n\right) & D^0_n \delta^c_n < \Delta u^t_n \leq D^1_n \delta^c_n \\ c^{max}_n \left(1 - D_{t/n}\right) \; ; & D^1_n \delta^c_n < \Delta u^t_n \leq \delta^c_n \\ 0 \; ; & \delta^c_n < \Delta u^t_n \\ E^{un}_n \, \Delta u^t_n \; ; & 0 \leq \Delta u^t_n < \max\left(\Delta u^t_n\right) \\ c^{t+}_n - \kappa {\Delta u^t_n}^2 \; ; & \Delta u^t_n \leq 0 \end{array} \right. \tag{5}$$

where Equation (5) correspond to the cohesive force during the opening loading stage, Equation (5)-5 corresponds to the elastic closing unloading/reopening reloading stage, and Equation (5)-6 corresponds to the case of $\Delta u^t_n < 0$ avoiding interpenetration of minerals. In Equation (5)-6, c^{t+}_n is the cohesion calculated with one of the Equation (5), and the parameter κ is a penalty coefficient whose value should be taken large to obtain physically relevant contacts avoiding mineral interpenetration of solid minerals ($\Delta u^t_n < 0$), but not too large for the numerical accuracy of the system of equations. In Equation (5)-1, the initial elastic normal stiffness E^0_n reads:

$$E^0_n = \frac{c_n}{\Delta u_n} = \frac{c^{max}_n \left(1 - D^0_n\right)}{D^0_n \delta^c_n} \tag{6}$$

The constant softening slope of interface cohesion is given by:

$$E^s_n = -\frac{c^{max}_n}{\delta^c_n} \tag{7}$$

Furthermore, for the standard interface cohesive model under elastic unloading (i.e., interface closing), the crack is fully closed[50] and the cohesion returns to zero following the relationship $c^t_n = E^{un}_n \; \Delta u^t_n$ (Equation (5)-5). The subsequent reloading follows the same path as illustrated in Figure 7. In Equation (5)-5, E^{un}_n is the elastic normal stiffness at unloading (closing) and reloading (reopening) stages and is defined by:

$$E^{un}_n = \frac{c^t_n}{\Delta u^t_n} \tag{8}$$

The above developments for the normal cohesive forces can be replicated to the tangential cohesive forces which develop under sliding Δu_t (tangential relative displacements) of solid minerals in contact. In this case, the tangential contact behaviour is symmetric for both sliding directions $\Delta u_t < 0$ and $\Delta u_t > 0$.

With the above equations, the mechanical behaviour of solid mineral contacts (interfaces), which are assumed as potential microcracks within the clay matrix and decohesion zones around mineral inclusions, is completely defined. The independent (unrelated) constitutive laws used for normal and tangential mechanical behaviours of mineral interfaces imply a decoupled relationship between them. Thus, both damage components can develop on the same mineral contact.

Although the dependence between the tangential and normal interface behaviours is not explicitly accounted for by the microscale cohesive model, the homogenised mechanical response of the mesoscale model (REA) can capture the mean stress dependence of the clay rock shear strength.[51]

4.2.2 | Elastoplastic model of clay aggregates

The plastic behaviour of the clay matrix and clay aggregates is modelled hereafter. In the following equations, compressive stresses and strains are considered negative according to the material mechanics sign convention. Under the assumption of small strains, the strain tensor of the clay aggregates at microscale can be decomposed into its elastic and plastic parts, denoted, respectively, by superscripts ^{e} and ^{p}:

$$\dot{\varepsilon}_{ij} = \dot{\varepsilon}^e_{ij} + \dot{\varepsilon}^p_{ij} \tag{9}$$

The elastic model is classical and the elastoplastic model used in this paper is taken from Abou-Chakra Guéry et al.[11] A modified Drucker-Prager yield criterion is used to model the shear strength of the clay aggregates. The yield function F_{ep} reads:

$$F_{ep}\left(\sigma_{ij}, \gamma^p\right) = q + \alpha^p \left(p - c_0\right) \tag{10}$$

where p is the mean stress, $q = \sqrt{\frac{3}{2} s_{ij} s_{ij}}$ is the equivalent deviatoric stress with s_{ij} the deviatoric parts of the stress tensor, c_0 represents the hydrostatic tensile strength related to material cohesion of the clay aggregates, and α^p represents their shear strength dependency to the mean stress level (internal friction parameter). The consistency condition enforces that the stress state always remains on the yield surface during plastic deformation: $F_{ep} = 0$ and $\dot{F}_{ep} = 0$. A higher compression with $p < 0$ will make F_{ep} more negative hence delay shear-induced yielding. Moreover, α^p is a hardening function depending on the internal variable γ^p, which is the equivalent deviatoric plastic strain (or plastic distortion), written as:

$$\alpha^p\left(\gamma^p\right) = \alpha^p_m - \left(\alpha^p_m - \alpha^p_0\right) \mathrm{e}^{-b\gamma^p} \tag{11}$$

$$\dot{\gamma}^p = \sqrt{\frac{2}{3} \dot{e}^p_{ij} \dot{e}^p_{ij}}; \quad \gamma^p = \int_0^t \dot{\gamma}^p \, d\tau \tag{12}$$

where e^p_{ij} denotes the deviatoric parts of the plastic strain tensor, $\dot{\mathrm{A}}$ is the rate of variable A, b controls the kinetics of the evolution of plastic hardening, $\dot{\gamma}^p$ is the rate of the equivalent deviatoric plastic strain, α^p_0 and α^p_m are the slopes of the initial yield and failure surfaces. Therefore, the hardening process is described by the variation of α^p from its initial threshold α^p_0 to its ultimate value α^p_m. A non-associated flow rule is considered here with the plastic potential, defining the direction of the plastic strain rate, defined as:

$$G_{ep}\left(\sigma_{ij}, \gamma^p\right) = q + \beta^p\left(\gamma^p\right) p \tag{13}$$

where $\beta^p(\gamma^p)$ is a parameter controlling plastic volumetric strain rate, and we have compressibility for $\beta^p \leq 0$ and dilatancy for $\beta^p > 0$. β^p is also a function of the hardening plastic variable γ^p:

$$\beta^p\left(\gamma^p\right) = \beta^p_m - \left(\beta^p_m - \beta^p_0\right) \mathrm{e}^{-b'\gamma^p} \tag{14}$$

where β^p_0 and β^p_m are the initial and final dilatancy parameters and b' controls the rate kinetics of the plastic volumetric strain. Such expressions of Equations (11) and (14) make the values of α^p and β^p vary within an increment of equivalent deviatoric plastic strain γ^p.

Using the expression of the plastic potential G_{ep}, the plastic strain rate is written as follows:

$$\dot{\varepsilon}_{ij}^{p} = \dot{\lambda}^{p} \frac{\partial G_{ep}}{\partial \sigma_{ij}} \tag{15}$$

where $\lambda^p \geq 0$ is the plastic multiplier and the volumetric $\dot{\varepsilon}_p^p$ and deviatoric $\dot{\varepsilon}_q^p$ plastic strain rates are defined by:

$$\dot{\varepsilon}_{p}^{p} = \dot{\lambda}^{p} \frac{\partial G_{ep}}{\partial p}; \quad \dot{\varepsilon}_{q}^{p} = \dot{\lambda}^{p} \frac{\partial G_{ep}}{\partial q} \tag{16}$$

Combining Equations (12), (15) and (16), the hardening variable can be formulated as:

$$\dot{\gamma}^{p} = \dot{\lambda}^{p} = \dot{\varepsilon}_{q}^{p} \tag{17}$$

The relation (17) is useful for the elastoplastic stress update in Appendix B.

4.2.3 | Elasto-viscoplastic model of clay aggregates

Similar to the elastoplastic part, under the assumption of small strains, the strain tensor of clay aggregates at microscale can also be decomposed into its elastic and viscoplastic parts, denoted, respectively, by superscripts ^{e} and ^{vp}:

$$\dot{\varepsilon}_{ij} = \dot{\varepsilon}_{ij}^{e} + \dot{\varepsilon}_{ij}^{vp} \tag{18}$$

The viscoplastic model for clay aggregates is established based on Perzyna's overstress concept[52] and Lemaitre's creep model.[53] The latter one is well documented and has an extensive experimental basis. The classic Lemaitre's model neglects the volumetric creep strain and uses an associated flow rule. Both of these points are not realistic for rock materials. We aim to revise these points in the present study.

For the viscoplastic yield function, we suggest the following form:

$$F_{vp} = \; q + \alpha^{vp}\, p - \sigma_{s} \tag{19}$$

where $\alpha^{vp} \geq 0$ is a model parameter quantifying the mean stress level sensitivity of the creep behaviour and σ_s is the creep threshold above which viscoplastic strains start to develop. The viscoplastic potential G_{vp} takes the following form:

$$G_{vp} = q + \beta^{vp} p \tag{20}$$

where $\beta^{vp} > 0$ corresponds to viscous dilatancy of rock and $\beta^{vp} < 0$ corresponds to viscous contraction. Then, the viscoplastic flow rule reads:

$$\dot{\varepsilon}_{ij}^{vp} = \dot{\lambda}^{vp} \frac{\partial G_{vp}}{\partial \sigma_{ij}} \tag{21}$$

where $\lambda^{vp} \geq 0$ is the viscoplastic multiplier and G_{vp} is the non-associated viscoplastic potential defining the direction of viscoplastic strain rate.

In practice for rocks, although contraction may be observed under small shear strain or before becoming dilatant at the beginning of creep tests,[54,55] creep dilatancy is still prevalent in most rocks. To reproduce the transition between creep contraction and dilation, β^{vp} should not be a constant but must vary from negative (contraction) to positive (dilation) values. Some authors mentioned the concept of variable dilatancy parameter for plasticity[56] as well as for viscoplasticity.[54] In this case, the dilatancy parameter can be defined as a function of the damage variables and the plastic deformation. However, this progressive change of dilatancy is out of the scope of this paper. In the following sections, β^{vp} will be considered to be a positive constant.

Inspired by Lemaitre's model, the viscoplastic multiplier $\dot{\lambda}^{vp}$ is defined as follows:

$$\dot{\lambda}^{vp} = \frac{1}{\eta} \left\langle \frac{F_{vp}}{\sigma_r} \right\rangle^{n} e^{-k\, \gamma^{vp}} \tag{22}$$

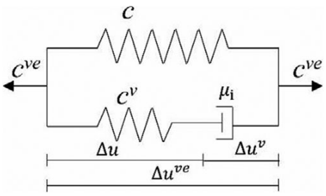

FIGURE 8 Schematic representation of the viscoelastic model of clay aggregate contacts.

where F_{vp} is the viscoplastic yield function, $\langle\ \rangle$ stands for the Macaulay's brackets with $\langle x\rangle = max(0, x)$, while η, n, k and σ_r are model parameters. The parameters $n \geq 1$ and $k \geq 0$ represent, respectively, the effect of stress intensity and strain hardening on the creep strain rate. The parameter η (in seconds) represents the clay aggregates viscosity and σ_r is a reference stress ($\sigma_r = 1$ MPa). The power form of the hardening variable γ^{vp-k} in the original Lemaitre's model is replaced by an exponential form $e^{-k\gamma^{vp}}$ after comparing their simulation results with experimental data from Armand et al.[12]

The viscoplastic distortion γ^{vp} (i.e., the equivalent deviatoric viscoplastic strain) is chosen as the hardening parameter:

$$\dot{\gamma}^{vp} = \sqrt{\frac{2}{3}\dot{e}^{vp}_{ij}\dot{e}^{vp}_{ij}} = \dot{\lambda}^{vp} \tag{23}$$

where $\dot{e}^{vp}_{ij}$ denotes the deviatoric part of the viscoplastic strain tensor. Nevertheless, if the material is viscoplastically incompressible, that is, $\beta^{vp} = 0$, this hardening variable is the same as for the original Lemaitre's model where the hardening variable is the accumulated deviatoric viscoplastic strain.

Injecting Equations (19), (20) and (23) into (21), the viscoplastic strain rate is finally expressed as follows:

$$\dot{\varepsilon}^{vp}_{ij} = \frac{1}{\eta}\left\langle \frac{q+\alpha^{vp}p-\sigma_s}{\sigma_r}\right\rangle^{n} e^{-k\,\gamma^{vp}}\left(\frac{3s_{ij}}{2q}+\frac{\beta^{vp}}{2}\delta_{ij}\right) \tag{24}$$

Note that the consistency condition does not apply for viscoplasticity; thus, the viscoplastic yield function can be positive $F_{vp} > 0$. When the current stress state is located outside the viscoplastic loading surface (overstress concept with $F_{vp} > 0$), viscoplastic deformations $\dot{\varepsilon}^{vp}_{ij} > 0$ are generated. The viscoplastic strain rate reduces with the accumulation of viscoplastic distortion γ^{vp} and can become null if the current stress state returns to the interior of the viscoplastic yield surface. Lastly, the thermodynamic consistency of the proposed viscoplastic model has to be verified. See Appendix A for the discussion of this part.

At each time step, the stresses and tangent operators for the elastoplastic and viscoplastic models need to be iteratively updated. These details can be found in Appendices B and C.

4.2.4 | Viscoelastic model of clay aggregates contacts

As aforementioned, another possible consideration of the clay rock viscosity is to add it into the microcracks within the clay matrix. Thus, the contact interfaces between elastic clay aggregates are assumed as viscoelastic. The corresponding rheological model, commonly denominated as the Standard Linear Solid model (SLS) or alternatively Zener model is represented in Figure 8. It consists of a damageable elastic spring (the top part in Figure 8) connected in parallel with one Maxwell element, composed of an elastic spring and a viscous dashpot (the bottom part in Figure 8). The behaviour of the damageable elastic spring is described using a bilinear interface cohesive model as shown in Figure 7. The total viscoelastic relative displacement $\Delta u^{ve}_{t/n}$ is the sum of the elastic and the viscous parts:

$$\Delta u^{ve}_{t/n} = \Delta u_{t/n} + \Delta u^{v}_{t/n} \tag{25}$$

and the total cohesive forces are the sum of the elastic and viscous cohesions:

$$c^{ve}_{t/n} = c_{t/n} + c^{v}_{t/n} \tag{26}$$

The relation between the elastic and the viscous cohesive forces is linked using a material parameter β, such as $c^{v}_{t/n} = \beta\, c_{t/n}$ leading to $c^{ve}_{t/n} = (1+\beta)\ c_{t/n}$. The evolution law for the viscoelastic opening and sliding is taken as:

$$\Delta \dot{u}^{v}_{t/n} = \frac{\delta^{c}_{t/n} c^{v}_{t/n}}{\mu_{t/n}} \tag{27}$$

where $\mu_{t/n}$ is the viscosity of the clay aggregate contacts (i.e., clay-clay interfaces). The derivation of the update of the cohesion and of the consistent tangent operator using recursive algorithm can be found in the work of Simo and Hughes.[57]

4.3 | Balance equation at mesoscale

The assumption of small strains at microscale makes the Cauchy stress tensor σ^{m}_{ij} approximately equals to the first Piola–Kirchhoff stress tensor P^{m}_{ij}. Moreover, gravity is neglected. Therefore, the momentum balance equation of the mesoscale BVP reads:

$$\frac{\partial \sigma^{m}_{ij}}{\partial x_j} = 0 \tag{28}$$

The principle of virtual work states that the system is in equilibrium if internal virtual work equals to external one. Considering an admissible virtual velocity field u^{*}_{i}, the weak formulation of Equation (28) reads:

$$\int_{\Omega} \sigma^{m}_{ij} \frac{\partial u^{*}_{i}}{\partial x_j} d\Omega = \int_{\Gamma^{+}_{int}} c^{+}_{i} u^{*,+}_{i} d\Gamma + \int_{\Gamma^{-}_{int}} c^{-}_{i} u^{*,-}_{i} d\Gamma \tag{29}$$

by considering the antiperiodic boundary tractions.

The mesoscale BVP is solved by discretising the REA and linearising the field equations with finite elements (FE). At the small scale, the solid constituents are modelled using two-dimensional four-node isoparametric quadrilateral FE with four integration points. For the contact interfaces between solid minerals, a four-node one-dimensional interface element is used with two integration points with initial zero thickness. A full Newton–Raphson iterative procedure is used to solve the boundary value problem numerically under the applied loading conditions. Moreover, the mechanical periodic boundary conditions of the REA (Equation (2)) are implemented by considering a penalty for the displacements of the homologous point (for example, a pair of points at x^{L} and x^{F} in Figure 5).

4.4 | Homogenisation of stress

The overall stress tensor over the REA results from the homogenisation process of the microscale stress tensor. Hill-Mandel principle of meso-homogeneity[58,59] allows to write:

$$\sigma_{ij} = \frac{1}{\Omega} \int_{\Gamma^{F}} t_i\, y_j\, d\Gamma \tag{30}$$

The corresponding homogenised consistent tangent operator is obtained by static condensation within the scheme of computational homogenisation.[35,37]

5 | ASSESSMENT OF MESOSCALE MODEL

In this section, numerical predictions from mesostructure calculations are compared with experimental data obtained on the COx claystone to examine the efficiency of the proposed model to reproduce the claystone creep deformations. To minimise the influence of mineralogical variability on experimental results, Armand et al.[12] performed triaxial and creep compression tests on COx claystone samples extracted from horizontal boreholes in the same geological horizon and in

TABLE 1 Microscale elastoplastic parameters of solid mineral constituents and their damageable contacts.

Materials				**E (GPa)**			**υ (−)**
Tectosilicates (quartz)				95			0.074
Carbonates (calcite)				84			0.317
Heavy minerals (pyrite)				305			0.154
Clay matrix				2.3			0.110
Clay aggregates	**α_m^p**	**α_0^p**	**b**	**c_0 (MPa)**	**β_0^p**	**β_m^p**	**b'**
	3.0	0.1	300	14	0	0.8	300
Interfaces	**$\delta^c_{t/n}$ (−)**	**$D^0_{t/n}$ (−)**	**$D^1_{t/n}$ (−)**	**c_t^{max} (MPa)**	**c_n^{max} (MPa)**		
	0.1	0.001	0.01	2.5	1.0		

the same area of the Andra's URL. The results of the numerical modelling are compared hereafter to these experimental data. It should be noted that the calibration of the parameters in the model is based on limited experimental data, which means that the uniqueness of the calibration cannot be guaranteed. Concerning the numerical modelling, morphologically representative mesostructures are firstly generated. Unless otherwise specified, several morphological characteristics of the mesostructures (REAs) are fixed: the mineral contents of quartz, carbonates, pyrite and clay are considered as being their average values in the COx clay-rich unit of 18%, 30%, 2% and 50%, respectively; the preferential orientation of mineral inclusions is parallel to the (quasi-)horizontal bedding planes; the angularity and elongation of mineral inclusions reproduce their morphology according to experimental evidences[18–20] and previous generations of morphologically representative mesostructures.[48] Then, mesoscale deviatoric compression tests and creep tests are numerically reproduced. The elastoplastic part of the model is first evaluated, followed by the viscous part of the models of clay aggregates and of their contacts. Note that the elastoplastic and viscoplastic models of clay aggregates are two separate models, both of which have no influence on each other. Lastly, the mechanical material response and the time-evolution of creep strain is analysed. The influence of several microscale characteristics on the mesoscale mechanical material response is studied through sensitivity analyses, followed by the study of temporal evolution of interface damage state.

5.1 | Elastoplastic modelling of claystone

The accuracy of the elastoplastic modelling of the clay aggregates (Section 4.2.2) is assessed in this section by modelling the material stress-strain behaviour for validation against experimental results. The mineral inclusion behaviours are considered as being elastic and all mineral contact behaviours are modelled with the cohesive model (Section 4.2.1). The elastic parameters of the minerals as well as the strength and damage parameters of their contacts have been calibrated by van den Eijnden[51] and Pardoen et al.,[48] based on the results of triaxial compression tests, and are listed in Table 1. However, the plastic parameters of the clay aggregates remain to be calibrated to reproduce the stress-strain behaviour of the clay rock.

Previous results have shown that the heterogeneity of the clay rock mesostructure with spatial variability of the mineral inclusions (random positions) has an influence on the overall response of different mesostructures subjected to deviatoric loading.[48] Therefore, several mesostructures of the COx claystone are generated and mechanically solicitated with 2D biaxial (deviatoric) compression tests. 10 REAs (an experienced value from Pardoen et al.[48]) of 100 × 100 μm are randomly generated with the same morphological characteristics of the mineral inclusions (granulometry, elongation, angularity and preferential orientation). An example is given in Figure 10B. A confining pressure of $\sigma_{11}^M = 12$ MPa is applied on the REAs which corresponds to the amplitude of the in situ stress at the median depth of the COx formation. Therefore, this confining pressure has been considered in all the compression tests presented hereafter. The isotropic confining phase is followed by a deviatoric loading phase, with controlled global (homogenised) vertical strain rate (strain rate of$\dot{\varepsilon}_{22}^M = 3.5{*}10^{-6}\ \mathrm{s}^{-1}$) and constant lateral stress σ_{11}^M.

The numerical results of the global mechanical responses of the mesostructures are detailed in terms of deviatoric homogenised stress q^M versus homogenised strains curves in Figure 9. They are compared to experimental data (from Armand et al.[12]; Pardoen and Collin[3]). The variability of the rock mechanical response at mesoscale (as observed by Pardoen et al.[48]), due to the mesostructural mineral spatial variability, is visible and only the range of the response curves is shown from most and least resistant responses. The plastic parameters of the clay aggregates are calibrated, as it was done for other micromechanical properties,[48] on a set of several mesostructures and by considering their average mechanical

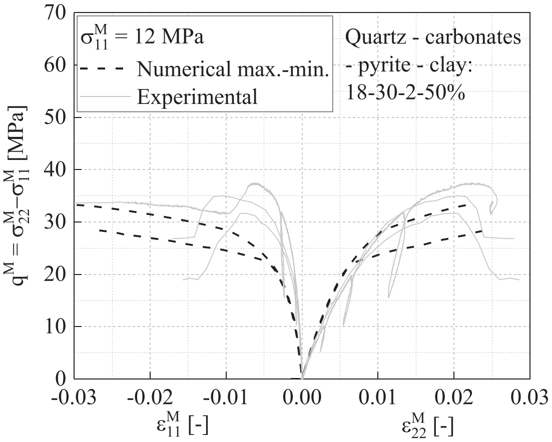

FIGURE 9 Variability of clay rock mechanical responses at mesoscale under biaxial compression.

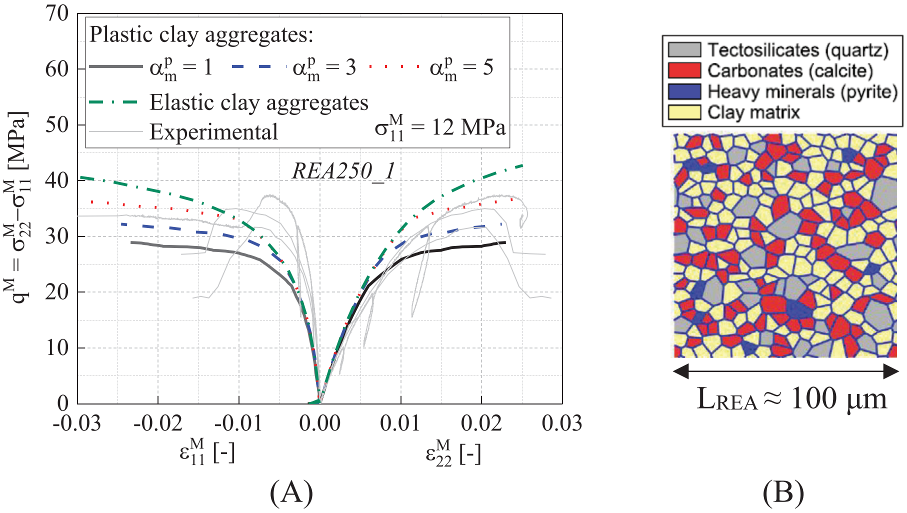

FIGURE 10 Influence of the internal friction parameter α_m^p of the clay aggregates (A) on the clay rock mechanical responses of (B) one mesostructure under biaxial compression.

response. The average response is represented in terms of the maximum deviatoric stress in stress-strain curves or the creep strains at the end of computation in strain-time curves, assuming it is representative of the material. The calibrated plastic parameters are listed in Table 1.

It should be noted that a 2D case is simulated at mesoscale to reproduce the experimental data from macroscale triaxial compression test. The numerical results concern individual REAs and interactions of different REAs at macroscale are therefore not included. Thus, the comparison is meaningful only for homogeneous modes of deformation (before the peak-deviatoric stress in stress-strain curves and before tertiary creep stage in strain-time curves). Macroscale non-homogeneous deformation modes, induced for example by strain localisation or fractures, will lead to structural responses which cannot be compared directly to the constitutive behaviour. Moreover, the macroscale responses exhibit a much more pronounced softening behaviour than the constitutive responses due to the macroscale non-homogeneous deformation. The comparison of the results after the peak stress (in the strain softening stage) is feasible in the case of a simulation at the scale of laboratory specimen by conducting FE^2 simulations, which is out of the scope of this paper.

Figure 9 shows the evolution of the deviatoric homogenised stress q^M with the vertical homogenised strain ε_{22}^M during the loading. A certain degree of variation exists in the material response from the most resistant samples to the least resistant ones due to the variability of the mesostructure. Figure 10A enlightens the influence of the slope of the failure surface α_m^p on the $q^M - \varepsilon_{22}^M$ response curve for one mesostructure under biaxial compression. The selected mesostructure shown in Figure 10B and labelled REA250_1 allowed to calibrate the clay plastic parameters of Table 1. This plastic parameter α_m^p defines the dependency of the clay aggregates shear strength on their mean stress level (internal friction parameter), at the end of the clay hardening. From Equations (10) and (11), a smaller value of α_m^p means that the material yields at a lower deviatoric stress, leading to higher plastic deformations in the clay matrix at the same level of deviatoric loading. Thus, a reduction of this plastic parameter causes a reduction of the mesostructure overall shear strength q_{max}^M as well as an increase of the mesostructure overall deformation. This is visible in the response curves in Figure 10A. On the contrary, a large value of α_m^p corresponds to an increase of the clay matrix shear strength and a reduction of its plastic deformation. An increase of this parameter increases the rock overall shear strength q_{max}^M and reduces its overall deformation (under the same deviatoric stress level). This delays the clay rock overall deformation, for example, ε_{11}^M and ε_{22}^M, at which the effect of the clay matrix plastic strain becomes dominant in the overall stress-strain behaviour (Figure 10A). Furthermore, if the plastic deformation of the clay aggregates is not considered, by assuming that they are elastic, the overall non-linearity of the microstructure behaviour is due to the initiation and development of micro-damage.

5.2 | Viscous modelling of clay aggregates and of their contacts

The viscous behaviour of the clay rock is now considered. The behaviour of mineral inclusions remains elastic while that of the contacts around them (i.e., contacts between inclusions or between an inclusion and the clay matrix) is still described by the cohesive model (Section 4.2.1). However, the creep behaviour of the clay matrix within the COx claystone is added. It is introduced by two microscale viscous mechanisms: the elasto-viscoplasticity of the clay aggregates (Section 4.2.3) or the viscoelasticity of their contacts (Section 4.2.4) studied separately.

The statistical averages of mineral contents in the COx clay-rich unit are again represented in numerical mesostructures of size 100 × 100 μm. The viscoplastic parameters of the clay aggregates and the viscoelastic parameters of their contacts remain to be calibrated to reproduce the creep behaviour of the clay rock. Similarly, to macroscale creep tests on laboratory specimen, the numerical simulations (in 2D) of creep tests under deviatoric loading on clay rocks consist of three stages. Firstly, the sample is subjected to an isotropic confining loading $\sigma_{11}^M = \sigma_{22}^M = \sigma_{ini}^M$. Secondly, the confining pressure σ_{11}^M is then kept constant and the axial stress σ_{22}^M is gradually increased until the designed deviatoric stress $q^M = \sigma_{22}^M - \sigma_{11}^M$ is reached. Lastly, the creep deformation occurs in the third stage, during which the confining stress σ_{11}^M and the axial stress σ_{22}^M, and thus the deviatoric stress q^M, are kept constant for a period of time.

5.2.1 | Elasto-viscoplastic modelling of clay aggregates

In this case, the clay aggregates are elasto-viscoplastic (Section 4.2.3) and the inter-aggregate contacts are modelled with the damageable cohesive interface model (Section 4.2.1). The calibration of the viscoplastic parameters is, as previously (Section 5.1), realised by considering the average mechanical response of a set of several mesostructures (10 REAs used in Section 5.1). In Equation (20), β^{vp} is a volumetric deformation parameter. Considering the very small dilatancy of clay rocks,[3] we fix the value of $\beta^{vp} = 0$. This is a simplifying assumption in which the phenomenon of progressive transition from contractive to dilative behaviour of most rocks is neglected. The viscoplastic stress threshold σ_s, in Equation (19), above which creep strain develops in clay aggregates should be a small-scale parameter which is not known. At macroscale, its determination is very difficult and it is closely linked to the duration of observation and to the confining pressure.[60] Some previous experimental results[43] suggest that the viscoplastic stress threshold should be lower than 2 MPa for the long-term creep behaviour of clay rock. Souley et al.[61] suggests that creep may take place beyond a threshold of 3 to 5 MPa based on the results of creep tests on COx claystone, and Mánica et al.[60] gives the threshold as 4 MPa in their study. A value of $\sigma_s = 3$ MPa is considered. Furthermore, in Equation (22), the parameter η represents the clay aggregates viscosity and n controls the rates (slope of the time evolution curve) of the viscoplastic strain for a short period of time as well as the difference in strain magnitude when different deviatoric stress levels are applied under the same confining pressure. Then, the parameter k controlling the hardening effect influences the viscoplastic strain rate at larger times. The calibrated viscoplastic parameters are listed in Table 2.

The variability of deviatoric homogenised stress q^M is first shown in Figure 11A in this case. Figure 11B shows the geometrical configuration of the mesostructured REA250_1 exhibiting an average numerical material response. Compared with Figure 9, the peak strengths increase obviously and are more consistent with laboratory results. Then, creep experiments under $\sigma_{11}^M = 12$ MPa of confining pressure and for different deviatoric stress levels, $q^M/q_{max} = 50\%$, 75% and 90%,[12] are numerically reproduced. The statistical mean value of the maximal deviatoric stress that the clay rock

TABLE 2 Microscale parameters of viscoplastic clay aggregates and damageable mineral contacts.

Clay aggregates	**η (s)**	**α^{vp}**	**β^{vp}**	**σ_s (MPa)**	**n**	**k**
	$9.8*10^{12}$	0.1	0	3	4.62	260
Interfaces	**$\delta^c_{t/n}$ (−)**	**$D^0_{t/n}$ (−)**	**$D^1_{t/n}$ (−)**	**c_t^{max}(MPa)**		**c_n^{max}(MPa)**
	0.1	0.001	0.01	2.5		1.0

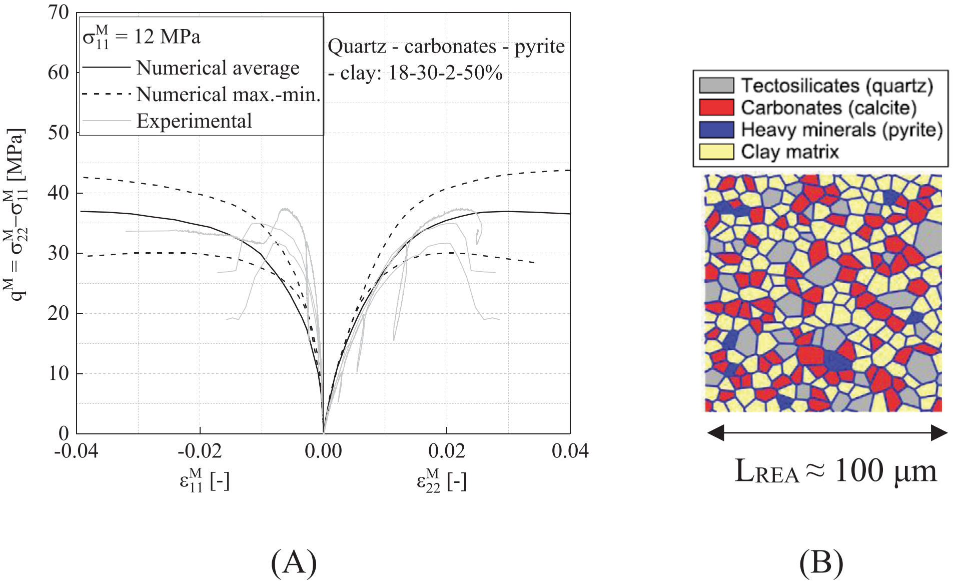

FIGURE 11 Variability of clay rock mechanical responses at mesoscale under biaxial compression (left) and reference REA with average numerical material response (right).

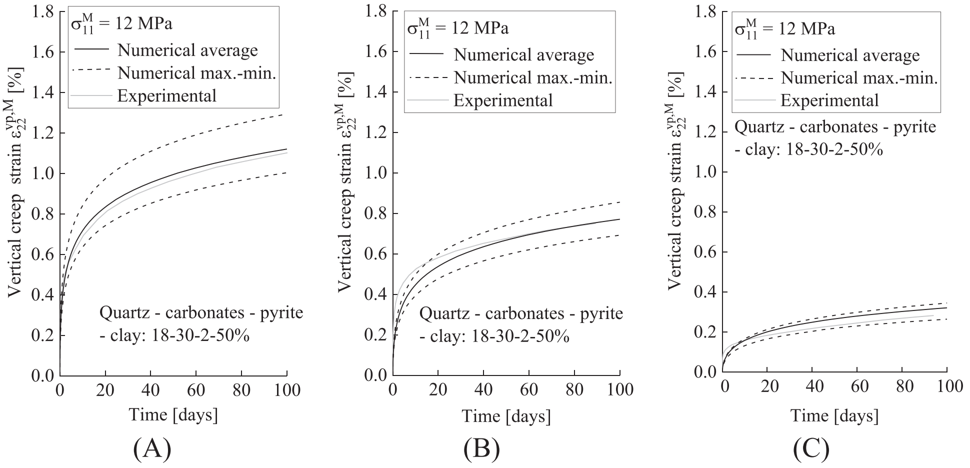

FIGURE 12 Variability of clay rock mechanical creep response at mesoscale during biaxial creep tests for three deviatoric stress levels q^M/q_{max} = (A) 90%, (B) 75%, (C) 50% in which q_{max} = 34.9 MPa.

can sustain q_{max} = 34.9 MPa,[12] that is, its shear strength, under 12 MPa of confining pressure is used as a reference for the creep experiments. A comparison of numerical and experimental evolution of vertical strains during the creep stage is shown in Figure 12 at different stress levels of q^M/q_{max} = 50%, 75% and 90%, corresponding to thus q^M = 17.5 MPa, 26.2 MPa and 31.4 MPa. After parameter calibration of η, α^{vp}, n and k (Table 2), one can observe that the numerical model reproduces well the strain evolution (i.e., the vertical homogenised creep strain $\varepsilon^{vp,M}_{22}$) of the COx claystone over time. As for previous modelling, a variability of the rock mechanical response, related to the mineral spatial variability at mesoscale, is obtained. In fact, with identical mineral contents, the Voronoï tessellation allows to generate periodic

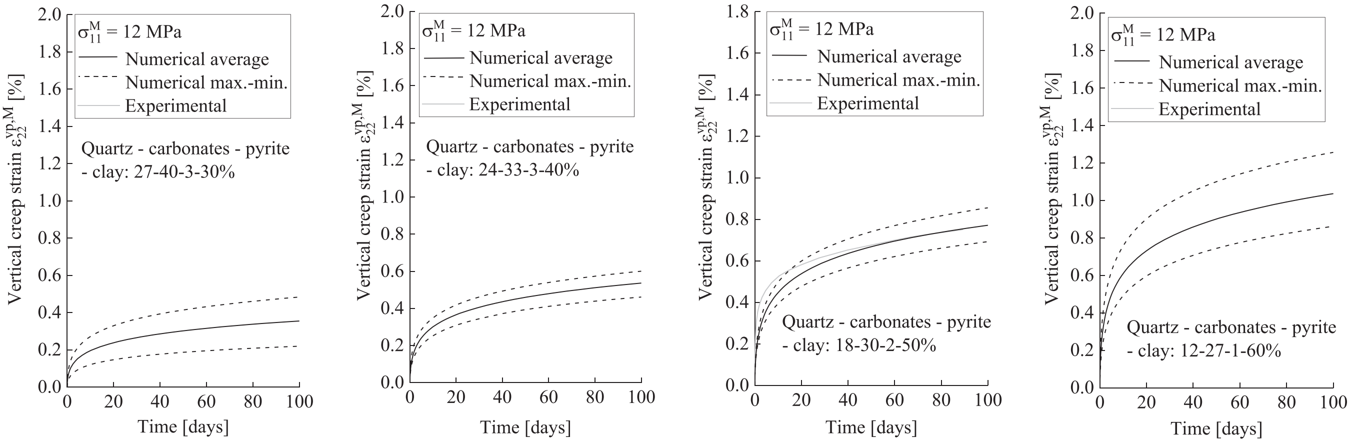

(A) (B) (C) (D)

FIGURE 13 Variability of clay rock mechanical creep response at mesoscale during biaxial creep tests considering viscoplastic clay aggregates, under a constant deviatoric stress level of q^{M}/q_{max} = 75%, for four proportions of clay mineral contents: (A) 30%, (B) 40%, (C) 50% and (D) 60% of clay.

2D REAs with random mesostructures (i.e., random positions of mineral inclusions), which is one of the origins of the mesoscale behaviour scattering.[48]

This influence of the mesostructure spatial variability can be observed in Figure 12, leading to a range of creep material response for each deviatoric stress level. As previously, only the range of the response curves is shown from most and least development of viscous strain with time. The mesostructured REA250_1 shown in Figure 11B exhibits an average numerical creep material response. It allowed to calibrate the viscoplastic parameters of the clay aggregates. This mesostructure is considered as a reference REA for the following sensitivity analyses, small-scale damage state analyses, and double-scale numerical simulation. Furthermore, the deviatoric stress level has a significant influence on the creep behaviour, as depicted in Figure 12A–C. A higher constant deviatoric stress engenders a larger development of creep strain with time, as observed experimentally.

Sensitivity analyses on creep deformation

In this section, the influence of several mesostructure properties and viscoplastic parameters on the creep behaviour of the COx claystone is investigated. Firstly, the clay content variation is considered. Experimental studies have shown that a certain variability of the mineralogical composition exists within the COx claystone.[5,12,18–20] It is expected that a larger clay content will produce larger creep deformation, due to its viscous nature. To enlighten this, REAs with the same characteristic length ($L_{REA} \approx 100$ μm) but different clay contents of 30%, 40%, 50% and 60% are considered. For each clay content, creep tests are modelled on 10 REAs under constant confining pressure of $\sigma_{11}^{M} = 12$ MPa and deviatoric stress level of $q^{M}/q_{max} =$ 75%. The results are shown in Figure 13 and compared to experimental measurements on a macroscale sample from the clay-rich unit of the COx claystone, thus for 50% of clay mineral content (Figure 13C). As expected, the homogenised creep strains become greater as clay content increases. The average REA vertical creep strains for these four mineral content cases at 100 days of creeping are, respectively, $\varepsilon_{22}^{vp,M}$ = 0.36%, 0.54%, 0.77% and 1.04%. The increase of the vertical creep strain as a function of the clay mineral content is represented in Figure 14. A quasi-linear relation can be found between the vertical creep strain and the clay mineral content for the configurations considered here. It seems that under a deviatoric stress level of 75% of the rock shear strength (under $\sigma_{11}^{M} = 12$ MPa), each 10% increase in clay content increases the vertical creep strain by 0.23%.

Secondly, the influence of the characteristic size L_{REA} of the mesostructure is considered, for 50% of clay content. To study the influence of the mesostructure size on the material creep response, we generate REAs with an increasing number of Voronoï cells of 50, 100 and 250 numerical cells, corresponding to $L_{REA} \approx$ 50, 70 and 100 μm, respectively. The variability of the material responses, in term of vertical creep strain evolution during creep simulations, over 10 tested REAs for each case of mesostructure size is shown in Figure 15. One can observe that a range exists in the material response for each case. The response under the same model parameters and simulation conditions are similar but its variability decreases with the increase of the REA size. In fact, the larger the REA, the more representative this behaviour is. The partial lack of representativeness of small mesostructures can be avoided by increasing the REA size; however, this increases the

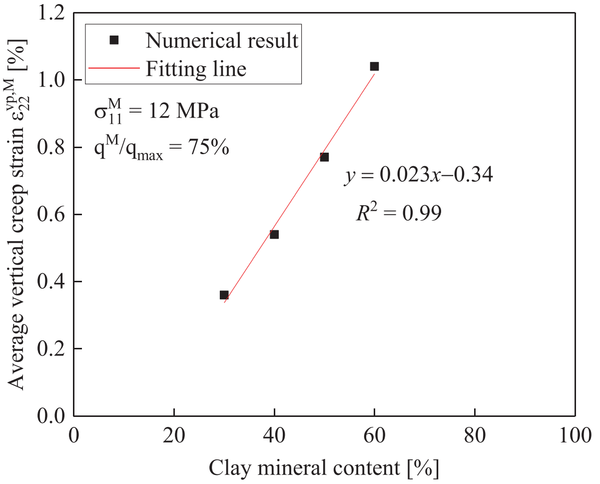

FIGURE 14 Influence of the clay mineral content on the average vertical creep strain, under a constant deviatoric stress level of $q^M/q_{max} \approx 75\%$, after 100 days of biaxial creep test.

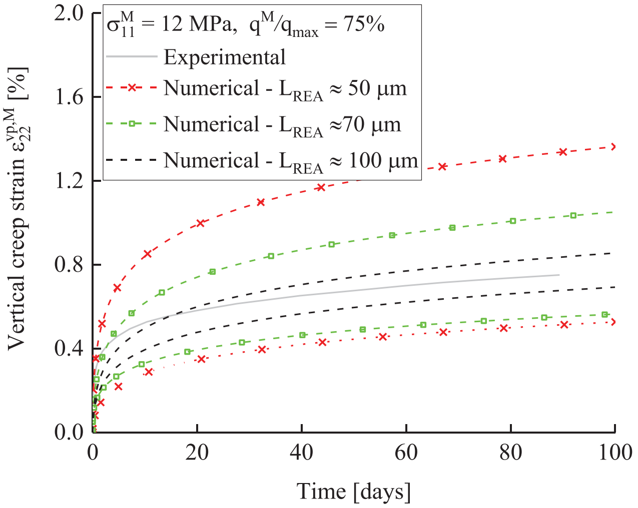

FIGURE 15 Variability of clay rock mechanical creep response due to different characteristic sizes of the mesostructure during biaxial creep test under a constant deviatoric stress level of $q^M/q_{max} = 75\%$.

computation time. The creep response dispersion of microstructures of 100 × 100 μm (250 cells) is relatively limited and is a good compromise between representativeness and computation time cost.[48]

The influence of viscous parameters of the clay aggregates is now considered. Figure 16A,B show the influence of the hardening parameter k and of the viscoplastic threshold σ_s on the creep deformation. In Figure 16A, it can be seen that reducing k engenders an increase of the creep strain rate and thus of the creep strain in the long term. Therefore, as aforementioned, the hardening parameter k can be determined by comparing the slope of creep strain curves in the long term between numerical and experimental results. In Figure 16B, as expected, larger values of the viscoplastic threshold σ_s generate lower viscous deformations. The vertical creep strain $\varepsilon_{22}^{vp,M}$ decreases from 0.9% to 0.67% after 100 days of creeping when the threshold increases from 0 to 5 MPa. The viscoplastic threshold has mainly an influence on the creep strain generated during a short time period because the curves are nearly parallel in the long term.

Creep-induced micro-damage of mineral contacts

Figure 17 illustrates the mesostructure (reference REA250_1) deformation and interface damage state for different times and vertical total strains, $\varepsilon_{22}^M = 0.89\%$, 1.9% and 2.6%. These strains correspond to the end of deviatoric compression phase, creep deformation after 1 year, and creep deformation after 100 years, respectively. The interface states (degrade, softening and full damage) are indicated by different colours and a larger symbol corresponds to the greater

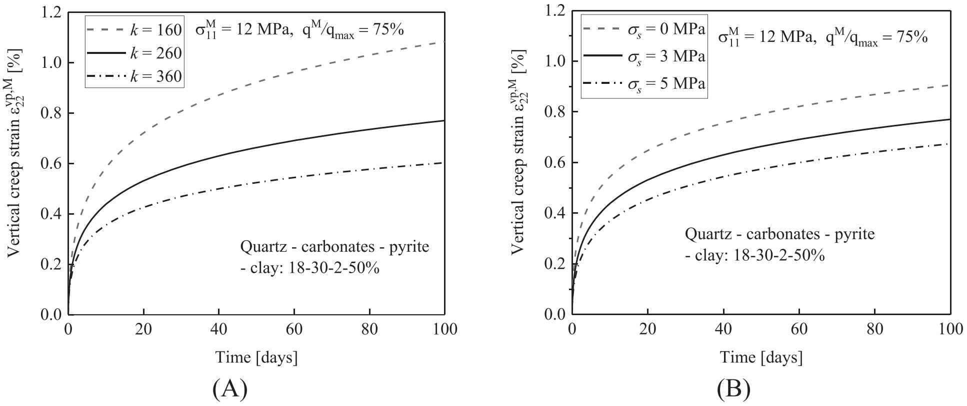

FIGURE 16 Influences of (A) the hardening parameter k and of (B) the viscoplastic threshold σ_s on the overall vertical creep deformation during biaxial creep test under a constant deviatoric stress level of q^M/q_{max} = 75%.

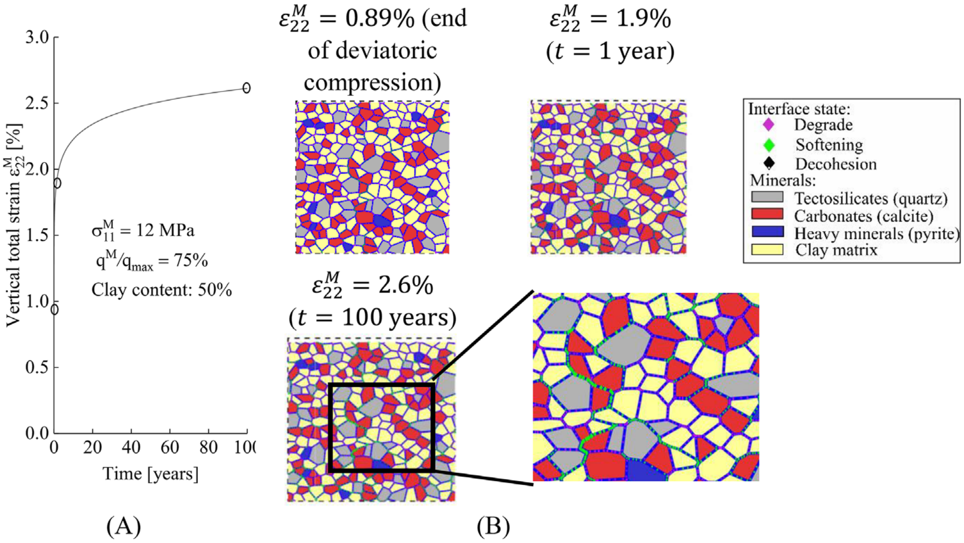

FIGURE 17 Evolution of clay rock damage at different vertical total strains under biaxial creep test: (A) material response and (B) patterns of mineral interface damage state.

interface relative displacements and damage. From Figure 17, one can observe that the interface damage can develop with time under constant stress conditions due to the viscosity of the clay aggregates. The creep deformation of clay aggregates leads to a gradual increase and accumulation of damage (i.e., cohesion softening) of the mineral contacts, as more mineral interfaces becomes partially damaged over time. Note that the damage develops preferentially in the interfaces around mineral inclusions rather than between the clay aggregates. Desbois et al.[21] have observed similar decohesion and microcrack developments, after shear failure tests, with analyses using a combination of SEM and broad ion beam (SEM-BIB). Two explanations can be envisaged: firstly, the stresses at the matrix-inclusion interfaces are higher than those between clay aggregates due to the higher contrast in stiffness (between the stiff mineral inclusions and the soft clay matrix), and therefore lead to larger relative displacements; the second reason is that only the clay aggregates generate creep deformation, and this tends to reduce substantially the stresses generated at the interface between clay aggregates, hence also their relative displacements. This increase of damage at the mineral contacts during material creeping, due to the clay matrix viscosity, might further lead to the development of microcracks (i.e., complete decohesion at mineral contacts, or fully damaged interfaces) for very large creep deformations in the long term.

In order to better investigate the creep-induced damage state of the mineral interfaces as shown in Figure 18, four indicators are introduced to quantify its development. The first indicator (Figure 18A) is the maximal values of damage in the tangential D_t^{max} and normal (opening) D_n^{max} directions among all interfaces. It is a local indicator which specifies when

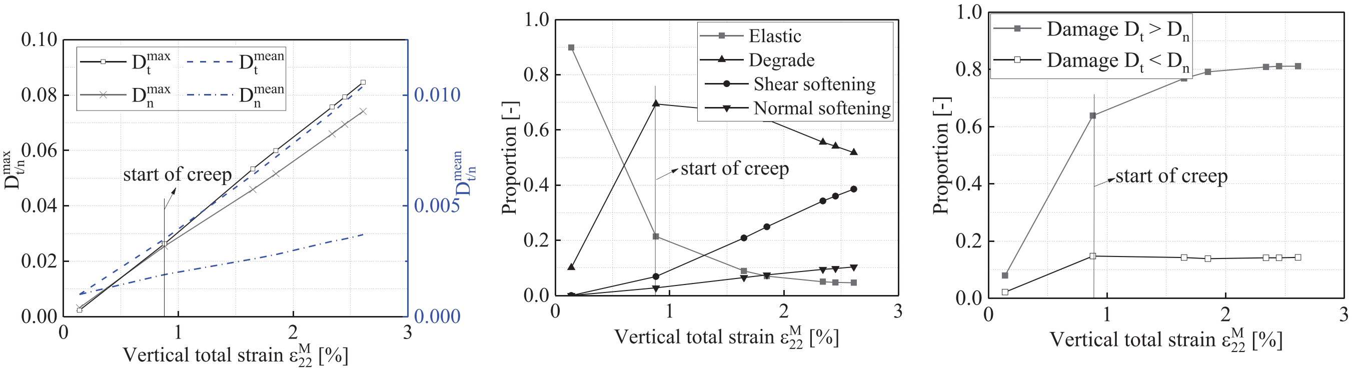

(A) (B) (C)

FIGURE 18 Indicators of the development of mineral interface damage state considering viscoplastic clay aggregates under biaxial creep test: (A) maximal and average interface damage in tangential and normal directions, (B) proportions to the total number of interfaces in different states and (C) proportions to the total number of interfaces undergoing more relative displacements in tangential or normal direction.

the most damaged mineral contact in a mesostructure starts to become partially damaged, in softening, or fully damaged. The second indicator (Figure 18A) $D_{t/n}^{mean}$ is the mean values of damage of all mineral interfaces in their two directions. It is a global indicator which reflects the average damage state of the mesostructure in shear or opening mode. The third indicator (Figure 18B) is the proportions to the total number of interfaces that are currently in the elastic ($D_{t/n} \leq D_{t/n}^0$), degraded ($D_{t/n}^0 < D_{t/n} \leq D_{t/n}^1$), softening in shear mode ($D_t^1 < D_t \leq 1$) and softening in opening mode ($D_n^1 < D_n \leq 1$). This indicator reflects the trend of the interfaces in different states and their quantity. The last indicator (Figure 18C) is the proportions to the total number of interfaces in the partially damage state (degrade and softening) which damage in the tangential direction is greater ($D_t > D_n$) or lower ($D_t < D_n$) than that in the opening direction. It allows to determine the dominant deformation and damage mode of the REA which can be in shear or in opening mode. The complete decohesion mode (D_t or $D_n > 1$) is not indicated here since no mineral interface have reached this state under the REA creep test.

The curves in Figure 18 start at the end of the isotropic compression, at which the proportions to the total number of interfaces in elastic, degrade, shear softening and open softening are, respectively, 89%, 10%, 0% and 0% (Figure 18B). It can be seen that at the end of the isotropic compression about one tenth of the interfaces have already undergone a certain relative displacement to reach the degrade state. Nevertheless, Figure 18A indicates that D_t^{max} (D_t^{mean}) is usually a bit larger than D_n^{max} (D_n^{mean}). This indicates that the generated relative displacement in the tangential direction of all mineral interfaces is larger than that in the normal direction in opening. This is because the REA is subjected to a deviatoric loading.

During the deviatoric loading, which is the second stage of the simulation, the proportions of interface damage state vary most significantly, for each damage state (Figure 18B). At the end of the deviatoric loading, the majority of the elastic interfaces becomes degraded and a small proportion already enters the shear softening and open softening states.

Afterwards, during the creep phase, the proportions of elastic and degraded interfaces and thus, the proportion of interfaces in softening regime increase. This indicates that the proportion of interfaces entering the degraded state from elasticity is smaller than the proportion of interfaces entering the softening state from the degraded state. During the creep phase (Figure 18B), the relative displacements occurring at the mineral contacts lead to a transition of the interface damage state from degraded to softening. At any time, a majority of the mineral interfaces undergo larger tangential relative displacement (Figure 18C).

The results of Figures 17 and 18 highlight that shearing is the dominant mode of deformation (relative movements) and damage at the mineral contacts. In fact, under deviatoric loading, shear deformations and tangential relative movements between mineral grains (at clay-clay aggregate, clay-inclusion and inclusion-inclusion contacts) are predominant.[48] As time increases during the creeping of the entire mesostructure of the clay rock, tangential sliding displacement and normal opening displacement of mineral contacts, especially at interfaces between clay aggregates and mineral inclusions, occur due to the creep deformation of the clay aggregates. Therefore, the internal damage accumulates and the creep deformation of the clay matrix can be a driving factor of time-dependent micro-damage processes.

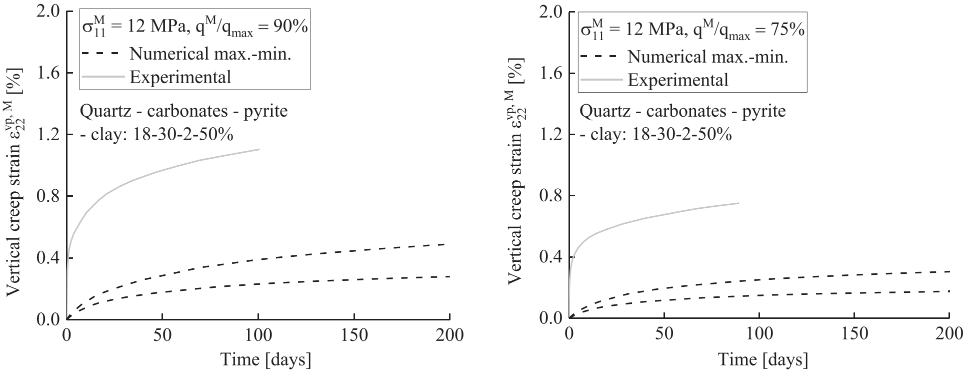

(A) (B)

FIGURE 19 Variability of clay rock mechanical creep response at mesoscale during biaxial creep tests considering viscoelastic clay aggregate contacts under two deviatoric stress levels of q^M/q_{max} = (A) 90% and (B) 75%.

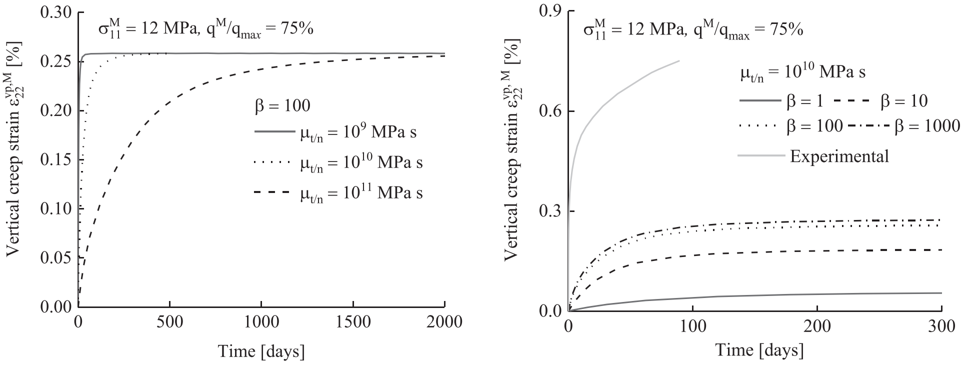

(A) (B)

FIGURE 20 Influence of (A) clay aggregate contact viscosity $\mu_{t/n}$ and (B) viscous parameter β on the vertical creep deformation under q^M/q_{max} = 75%.

5.2.2 | Viscoelastic modelling of clay aggregate contacts

In this approach, it is considered that the viscous behaviour of the clay rock, in the clay matrix, is related to the development of viscous relative displacements (i.e., a time-dependent sliding and opening) between large clay aggregates. The latter are considered as rigid elastic entities. As previously, the elastic parameters of the minerals as well as the parameters of their contacts are listed in Table 1. A biaxial creep test has been simulated on COx claystone mesostructures with viscous contacts between clay aggregates, that is, clay-clay interfaces. The creep test modelling has been performed on the 10 REAs of 100 × 100 μm having a 50% clay content, which have been used in Section 5.2.1. The modelling has been performed under a confining stress of $\sigma_{11}^M = 12$ MPa and under a deviatoric stress of $q^M/q_{max} = 75\%$ and 90%, thus $q^M = 26.2$ MPa and 31.4 MPa. Figure 19A,B show the time evolution of the vertical creep strain $\varepsilon_{22}^{vp,M}$ under two constant deviatoric stresses. When viscosity exists only in the contact between clay aggregates, one can observe that the overall (homogenised) vertical creep deformation $\varepsilon_{22}^{vp,M}$ generated by the viscosity is small compared to experimental data, in both short and long terms. The creep strains finally tend asymptotically towards constant values due to the used viscoelastic model, which corresponds to the secondary creep (creep deformation reaching a steady state). However, this behaviour may become different when the applied deviatoric stress is much closer to the peak stress. This will be discussed in the following.

Sensitivity analyses on creep deformation

The simulations are carried out on the same set of 10 mesostructures and only the average response of REAs (mesostructure REA250_1) is shown. Figure 20A,B illustrates the influence of the viscous parameters β and $\mu_{t/n}$. The simulation conditions and the other model parameters are the same as before. As expected, the viscosity of the clay aggregates contacts $\mu_{t/n}$ only influences the rate at which the creep deformation reaches a steady state (Figure 20A), not its final value.

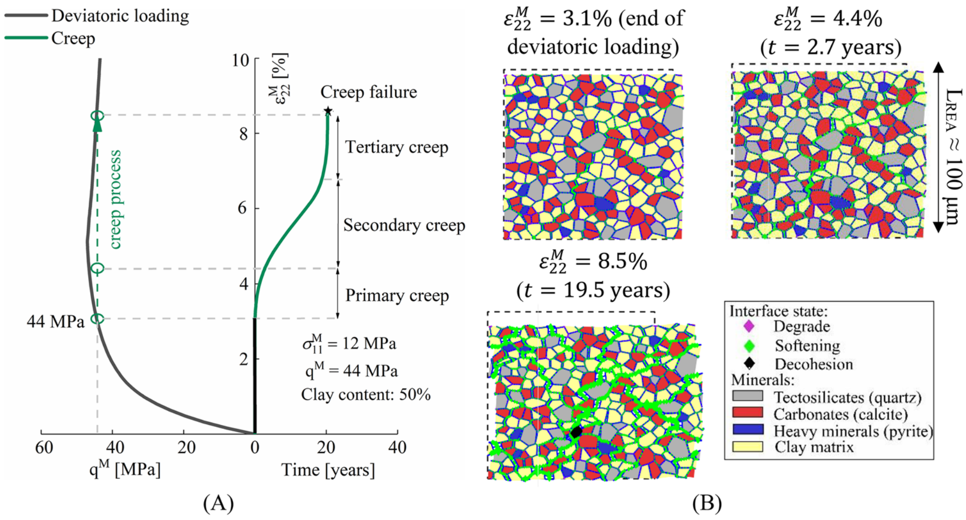

FIGURE 21 Creep stages and induced failure in clay rock during biaxial creep test considering viscoelastic clay aggregate contacts: (A) material response and (B) microscale damage and mesoscale cracking pattern induced by the material creep with time.

On the other hand, a larger value of the viscous parameter β leads to a larger vertical creep strain development; however, this effect reduces as the value of β increases. Note that the clay aggregate interface elastic stiffness also depends on β, which can be seen from Figure 8. However, A more realistic modelling of the clay aggregate contacts should consider their irreversible relative sliding and opening. This will be further investigated in future studies.

Creep-induced micro-damage of mineral contacts

The mesostructure REA250_1 (Figure 11B) is again considered with 50% of clay content, viscoelastic clay aggregate contacts and the following clay-clay interface parameters: $c_t^{max} = 0.025$ MPa, $c_n^{max} = 0.01$ MPa, $\delta^c_{t/n} = 0.1$, $D^0_{t/n} = 0.001$, $D^1_{t/n} = 0.01$, $\beta = 100$ and $\eta = 10^9$ MPa s. Under confining pressure of $\sigma^M_{11} = 12$ MPa and biaxial compression (loading rate of$\dot{\varepsilon}^M_{22} = 3.5*10^{-6}$ 1/s), the mesostructure deviatoric stress q^M versus axial strain ε^M_{22} response is visible in Figure 21A. Under this confining pressure, the maximal deviatoric stress (i.e., the shear strength) that the mesostructure can sustain is about $q^M_{max} = 47$ MPa. Then, a creep test is performed under constant confining pressure of $\sigma^M_{11} = 12$ MPa and deviatoric stress of $q^M = 44$ MPa.

A high value of the constant deviatoric stress is chosen close to the shear strength of the REA to study the possible damage induced by the creep. Three stages of creep can develop in viscous materials as clay rocks: a primary creep in the short term with a decrease of the creep strain rate (rate decelerating), a secondary creep with a stabilisation of the creep strain rate over time (steady state creep with constant rate), and a possible tertiary creep in the long term with an increase of the creep strain rate (rate accelerating) towards creep failure.[22] These three stages of creep developed by our model are shown in Figures 21A and 23A. The tertiary creep occurs for materials exhibiting a softening, damageable, or quasi-brittle behaviour, as dense soils, overconsolidated clays and rocks.[62] These three creep stages are also observed for the COx claystone during creep tests under triaxial compression conditions.[22] Even if it has been seldom observed in rocks, the increase of the creep rate appears to be related to the onset and development of damage.[22] The later can further lead to a creep-induced failure of the material.

Figure 21A illustrates both the evolution of the vertical total strain ε^M_{22} with the deviatoric loading and with time, which corresponds to the creep process. An interesting result is observed when the applied constant deviatoric stress (44 MPa) is close to the peak deviatoric stress (47 MPa): the third stage of creep (accelerated creep stage) which can lead to the creep failure is observed. Indeed, the creep deformation rate starts to increase after a time period of 16 year and then increases rapidly. Furthermore, the development of microscale damage and mesocracking pattern induced by the material creep with time is shown in Figure 21B, at the end of the deviatoric loading and during the accumulation of creep deformation. It is observed that the overall material damage at mineral contacts increases and that only a few interfaces reach full decohesion at the end of the creep, after 19.5 years. In fact, at the end of the creep, the complete decohesion appears in a localised manner for a small proportion of mineral contacts. Therefore, the creep strain development induces damage accumulation which leads to the initiation of the mesostructure cracking and failure. Similarly, tertiary creep with damage

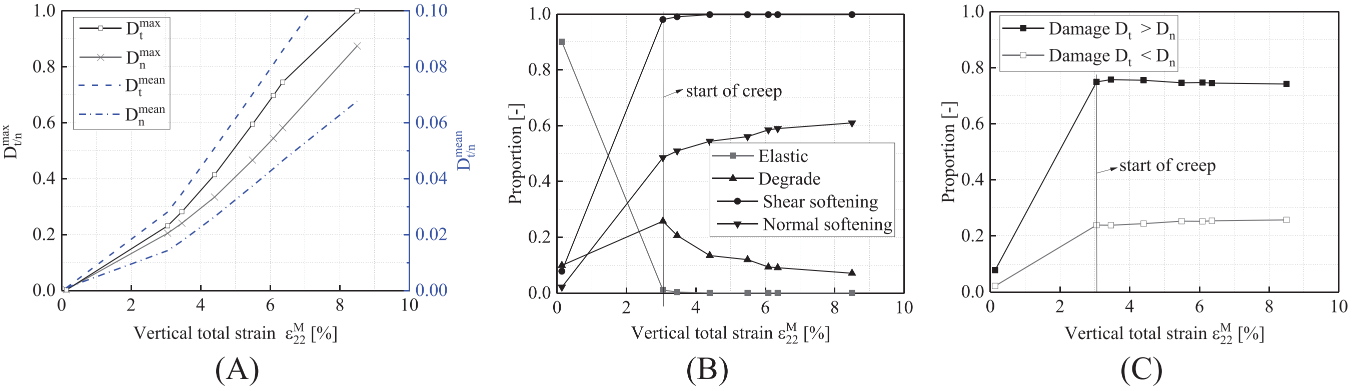

FIGURE 22 Indicators of the development of mineral interface damage state considering viscoelastic clay aggregate contacts under biaxial creep test: (A) maximal and average interface damage in tangential and normal directions, (B) proportions to the total number of interfaces in different states and (C) proportions to the total number of interfaces undergoing more relative displacements in tangential or normal direction.

accumulation and creep failure was observed during creep at macroscale in the COx claystone by Liu et al.[22] Numerically, the FE computation is performed until it fails to converge at the point of failure.

Four indicators, as described in Section 5.2.1, are analysed in Figure 22 to better investigate the creep-induced damage state of the interfaces between minerals for the results shown in Figure 21. As aforementioned, shearing is the dominant mode of deformation, relative movements and damage under deviatoric loading. Then, during creep stage after deviatoric compression, when viscosity exists at the contacts between clay aggregates, it implies an increase of the damage and relative displacements between mineral grains. This overall microscale damage increase was also observed for viscous clay aggregates (Section 5.2.1, Figure 18). Moreover, there are only 2 mineral interfaces (over a total of 1582 interfaces) that have reached the complete decohesion state in the tangential direction (black symbols in Figure 21B) after 19.5 years of creep. The microscopic damage induced by the creep is therefore very localised. These fully damaged contacts are not shown in Figure 22B due to their small proportion.

5.2.3 | Influence of viscous modes on tertiary creep and creep failure

Although tertiary creep has been rarely observed to date on clay rocks, it may occur and lead to claystone failure over time under certain conditions.[22] The possible occurrence of creep failure has been studied from a mesostructural perspective by considering the material heterogeneity at the mesoscale with various mineral spatial arrangement. To investigate the influence of the viscosity of the clay matrix (both of clay aggregates and of their contacts) on the overall creep deformation, several mesostructures are generated and submitted to a creep test with an applied constant deviatoric stress close to their peak stress value. Three REAs with 50% of clay content have been randomly generated with different heterogeneous mesostructures of 100 × 100 μm, labelled REA250_1, REA250_2 and REA250_3.

Hereafter, the viscosity of the clay aggregates and of their contacts is studied separately, considering either viscoplastic clay aggregates and damageable mineral contacts as in Section 5.2.1, either viscoelsatic clay aggregate contacts and elastic clay aggregates as in Section 5.2.2. For each mesostructure, the microscale constitutive parameters are the same as those used previously in Section 5.2.1. For the former mesostructure REA250_1, the effect of the viscosity of the clay aggregate contacts has already been studied and has led to tertiary creep and creep failure (Figure 21). Then, the viscosity of the clay aggregates is now considered. For the latter mesostructures REA250_2 and REA250_3, both viscosity types are considered. The deviatoric strengths of the mesostructures 1, 2 and 3 under biaxial compression with $\sigma^M_{11} = 12$ MPa (strain rate of$\dot{\varepsilon}^M_{22} = 3.5{*}10^{-6}\ \mathrm{s}^{-1}$) are, respectively, of $q^M_{max} = 47$ MPa, 46 MPa and 39.1 MPa. The applied constant deviatoric stresses during the creep phase are, respectively, of $q^M = 44$ MPa, 44 MPa and 37 MPa.

Figure 23 shows the relation between the evolution of the creep deformation (Figure 23A) and the micro-damage and mesocracking patterns induced by the viscosity of the clay aggregates (Figure 23B) or of their contacts (Figure 23C), for the three mesostructures. These patterns are shown, for each mesostructure, for a vertical total strain ε^M_1 inducing the mesoscale tertiary creep by one or the other mode of clay matrix viscosity. From the creep curves shown in Figure 23A,

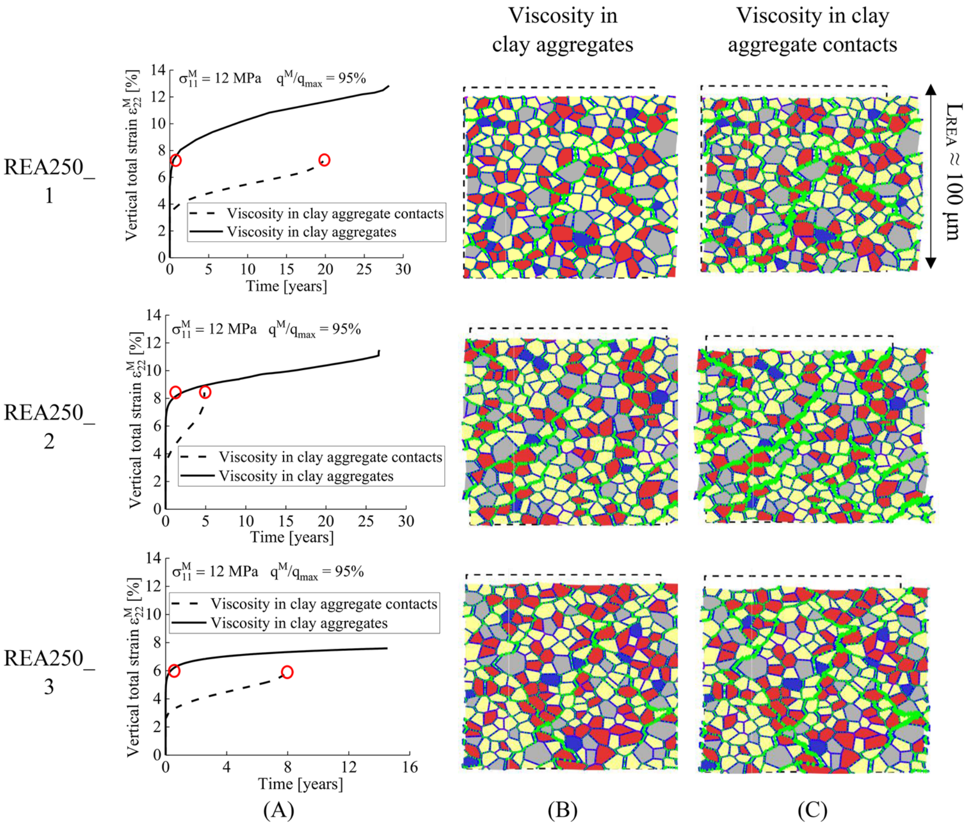

FIGURE 23 Relation between (A) creep deformation evolution under and (B,C) induced micro-damage and mesocracking patterns for several mesostructures when viscosity is considered in clay aggregates or at clay aggregate contacts.

one can observe that the viscosity in clay aggregates or in their contacts can both cause accelerated creep of the rock (e.g., mesostructures REA250_1 and REA250_2). Furthermore, under the same vertical total strains, the clay aggregate interface viscosity induces more damage between minerals in the mesostructure, which can be seen in terms of damage magnitude and distribution (Figure 23B,C). The analyses of the numerical results indicate that the viscosity at the clay aggregate contacts is more likely to cause rock damage and may have an important contribution to the creep-induced failure of the claystone.

6 | CONCLUSIONS

In order to investigate the time-dependent mechanical behaviour of heterogeneous clay rocks, the contribution of microscale viscous characteristics of minerals to the mesoscale creep behaviour of the COx claystone has been investigated. This has been achieved by micromechanical approach in which the clay rock is considered as a composite medium consisting of rigid elastic mineral inclusions (quartz, calcite and pyrite) embedded in a clay matrix.

At the microscale, the damage and failure modes have been reproduced by considering potential decohesion around mineral inclusions and potential microcracking within the clay matrix. The latter are modelled at the interfaces between solid mineral grains as damageable cohesive contacts. Considering the viscosity of the claystone, it is assumed to be originated from the time-dependent creep deformation of the clay matrix. Two origins have been considered: either viscous clay aggregates or viscous intergranular microfractures propagating in the clay matrix between rigid clay aggregates. Both viscous modes have been considered either by a viscoplastic behaviour for the clay aggregates or by a viscoelastic behaviour of the inter-clay aggregate contacts. The viscoplastic model of the clay aggregates, satisfying the thermodynamic consistency conditions, is based on Lemaitre's form, in which a mean stress dependence and a non-associated flow rule are introduced. The new hardening law based on an exponential function instead of a power law obtains a creep evolution that is more consistent with experiment results.

The contributions of the two considered microscale origins of the clay matrix viscosity to the mesoscale creep behaviour of the COx claystone have been both studied. The numerical results indicate that the viscosity, in both cases, has an influence on the overall creep deformation of the clay rock. Considering the viscosity in the clay aggregates allows to reproduce the time evolution of the COx claystone creep strain with a good agreement to experimental measurements from triaxial creep tests. Nevertheless, considering the viscosity at the contacts between clay aggregates generates a smaller creep deformation of the rock compared to experimental measurements. Furthermore, stress level and mineralogical composition affect the overall creep deformation of the claystone. Numerical results indicate that both high the deviatoric stress level and the high clay content increase the creep deformation, as observed by experimental studies. In the context of radioactive waste repositories in the COx claystone, it is therefore crucial to understand the phenomena involved during the long-term creep of the rock around the galleries excavated in the clay-rich lithostratigraphic unit. During material creep under deviatoric loading, shearing is the dominant mode of deformation and of relative displacement at the contacts between mineral grains. Creep-induced relative movements between mineral grains (at clay-clay aggregate, clay-inclusion and inclusion-inclusion contacts) occur mainly by sliding (i.e., tangential movements) along the interfaces, resulting in shear deformations inside the mesostructure.

A particular attention has to be paid to creep when it occurs at a high deviatoric stress level, for a long period of time and in an indurated clay rock which exhibits a quasi-brittle behaviour (softening behaviour). Under these conditions, an increase of the creep strain rate (tertiary creep) can occur and may lead to creep-induced failure. In addition to the first stages of creep (primary and secondary creep), this phenomenon of accelerated creep strain in the long term has also been reproduced and demonstrated numerically. Considering the material damage, creep deformation can be a driving factor of time-dependent microscale damage and cracking processes. It has been found that that creep strain development can induce the accumulation of damage at mineral grain contacts in a localised manner, leading to microcrack development. The microcracks induced by creep deformation tend to preferentially develop at the interfaces around mineral inclusions rather than between clay aggregates. Eventually, these phenomena lead to the initiation of mesostructure cracking and rock failure. Furthermore, both origins of viscosity can lead to creep failure of the claystone as long as the damage of contact interfaces between mineral grains reaches a certain damage level.

Furthermore, though numerical simulations can provide valuable insights and predictions, experimental observations and a deep understanding of the underlying physics are crucial to ensure the reliability and accuracy of any conclusions drawn from simulations.

ACKNOWLEDGEMENTS

The first author is supported by the China Scholarship Council (CSC) with a PhD Scholarship (File No. 202006560007) for his research work.

CONFLICT OF INTEREST STATEMENT

The authors declare no conflicts of interest.

DATA AVAILABILITY STATEMENT

Data will be made available on request.

ORCID

Yufeng Sun https://orcid.org/0000-0002-5015-9250

REFERENCES

1. Andra. *Dossier 2005 Argile. Synthesis: Evaluation of the Feasibility of a Geological Repository in an Argillaceous Formation, Meuse/Haute Marne Site*. Tech. Rep., Paris.; 2005.
2. Belmokhtar M, Delage P, Ghabezloo S, Conil N. Drained triaxial tests in low permeability shales: application to the Callovo-Oxfordian Claystone. *Rock Mech Rock Eng*. 2018;51:1979-1993.
3. Pardoen B, Collin F. Modelling the influence of strain localisation and viscosity on the behaviour of underground drifts drilled in claystone. *Comput Geotech*. 2017;85:351-367.
4. Mánica MA, Gens A, Vaunat J, Armand J, Vu M. Numerical simulation of underground excavations in an indurated clay using non-local regularisation. Part 1: formulation and base case. *Géotechnique*. 2021;72(12):1092-1112.
5. Armand G, Leveau F, Nussbaum C, et al. Geometry and properties of the excavation-induced fractures at the Meuse/Haute–Marne URL drifts. *Rock Mech Rock Eng*. 2014;47(1):21-41.

6. Bikong C, Hoxha D, Shao JF. A micro-macro model for time-dependent behavior of clayey rocks due to anisotropic propagation of microcracks. *Int J Plast*. 2015;69:73-88.
7. Farhat F, Shen WQ, Shao JF. A micro-mechanics based viscoplastic model for clayey rocks. *Comput Geotech*. 2017;89:92-102.
8. Huang Y, Shao JF. A micromechanical analysis of time-dependent behavior based on subcritical damage in claystones. *Int J Damage Mech*. 2012;22:773-790.
9. Pardoen B, Levasseur S, Collin F. Using local second gradient model and shear strain localisation to model the excavation damaged zone in unsaturated claystone. *Rock Mech Rock Eng*. 2015a;48(2):691-714.
10. Pardoen B, Seyedi DM, Collin F. Shear banding modelling in cross-anisotropic rocks. *Int J Solids Struct*. 2015b;72:63-87.
11. Abou-Chakra Guery A, Cormery F, Shao JF, Kondo D. A multiscale modeling of damage and time-dependent behavior of cohesive rocks. *Int J Numer Anal Methods Geomech*. 2009;33:567-589.
12. Armand G, Conil N, Talandier J, Seyedi DM. Fundamental aspects of the hydromechanical behaviour of Callovo-Oxfordian claystone: from experimental studies to model calibration and validation. *Comput Geotech*. 2017;85:277-286.
13. Sun YF, Weng XL, Wang WL, Niu HS, Li H, Zhou RM. A thermodynamically consistent framework for visco-elastoplastic creep and anisotropic damage in saturated frozen soils. *Contin Mech Thermodyn*. 2021a;33:53-68.
14. Sun YF, Wong H, Pardoen B, Deleruyelle F, Dufour N. Long-term hydromechanical behaviour of a deep cavity taking into account a simplified sequence of life stages. *Comput Geotech*. 2023;156:105256.
15. Zhao JJ, Shen WQ, Shao JF, Liu ZB, Vu MN. A constitutive model for anisotropic clay-rich rocks considering micro-structural composition. *Int J Rock Mech Min Sci*. 2022;151(1):105029.
16. Bui TA, Wong H, Deleruyelle F, Xie LZ, Tran DT. A thermodynamically consistent model accounting for viscoplastic creep and anisotropic damage in unsaturated rocks. *Int J Solids Struct*. 2017;117:26-38.
17. Sun YF, Wong H, Pardoen B, et al. Analytical study of post-closure behaviour of a deep spherical cavity in a dilatant viscoplastic rock mass. *Comput Geotech*. 2021b;139(3):104419.
18. Cosenza P, Prêt D, Giraud A, Hedan S. Effect of the local clay distribution on the effective elastic properties of shales. *Mech Mater*. 2015a;84:55-74.
19. Cosenza P, Prêt D, Zamora M. Effect of the local clay distribution on the effective electrical conductivity of clay rocks. *J Geophys Res Solid Earth*. 2015b;120:145-168.
20. Robinet JC, Sardini P, Coelho D, et al. Effects of mineral distribution at mesoscopic scale on solute diffusion in a clay-rich rock: example of the Callovo Callovo–Oxfordian mudstone (Bure, France). *Water Resour Res*. 2012;48(5):W05554.
21. Desbois G, Höhne N, Urai JL, Bésuelle P, Viggiani G. Deformation in cemented mudrock (Callovo-Oxfordian Clay) by microcracking, granular flow and phyllosilicate plasticity: insights from triaxial deformation, broad ion beam polishing and scanning electron microscopy. *Solid Earth*. 2017;8(2):291-305.
22. Liu ZB, Shao JF, Xie SY, Conil N, Zha WH. Effects of relative humidity and mineral compositions on creep deformation and failure of a claystone under compression. *Int J Rock Mech Min*. 2018;103:68-76.
23. Mitchell JK, Soga K. *Fundamentals of Soil Behavior*. John Wiley & Sons; 2005.
24. Bertrand F, Buzzi O, Bésuelle P, Collin F. Hydro-mechanical modelling of multiphase flow in naturally fractured coalbed using a multiscale approach. *J Nat Gas Sci Eng*. 2020;78:103303.
25. Borja RI, Yin Q, Zhao Y. Cam-Clay plasticity. Part IX: on the anisotropy, heterogeneity, and viscoplasticity of shale. *Comput Methods Appl Mech Engrg*. 2020;360:112695.
26. Choo J, Semnani SJ, White JA. An anisotropic viscoplasticity model for shale based on layered microstructure homogenization. *Int J Numer Anal Methods Geomech*. 2020;45(4):502-520.
27. Mourlas C, Pardoen B, Bésuelle P. Large-scale failure prediction of clay rock from small scale damage mechanisms of the rock medium using multiscale modelling. *Int J Numer Anal Methods Geomech*. 2023:1-3. doi:10.1002/nag.35
28. Nguyen K, Desrues J, Vo T, Combe G. FEM×DEM Multi-scale model for cemented granular materials: inter- and Intra-granular cracking induced strain localization. *Int J Numer Anal Methods Geomech*. 2020;46(5):1001-1025.
29. Semnani SJ, White JA. An inelastic homogenization framework for layered materials with planes of weakness. *Comput Methods Appl Mech Eng*. 2020;370:113221.
30. Shen WQ, Shao JF. A micro–macro model for porous geomaterials with inclusion debonding. *Int J Dam Mech*. 2014;24(7):1026-1046.
31. Shen WQ, Shao JF. A micromechanical model of inherently anisotropic rocks. *Comput Geotech*. 2015;65:73-79.
32. Zhou C, Qian JG, Yin ZY, Liu YJ, Du ZB. Effect of particle shape and bedding angle on suffusion in gap-graded granular soils by coupled CFD-DEM method. *Int J Numer Anal Methods Geomech*. 2023;47:1373-1398. doi:10.1002/nag.3519
33. Weng XL, Li H, Hu JB, Li L. Behavior of saturated remolded loess subjected to coupled change of the magnitude and direction of principal stress. *Int J Geomech*. 2023;23(1):04022244.
34. Feyel F, Chaboche JL. FE2 multiscale approach for modelling the elastoviscoplastic behaviour of long fibre SiC/Ti composite materials. *Comput Methods Appl Mech Eng*. 2000;183(3–4):309-330.
35. Kouznetsova V, Brekelmans WAM, Baaijens FPT. An approach to micro-macro modeling of heterogeneous materials. *Comput Mech*. 2001;27(1):37-48.
36. Schröder J. A numerical two-scale homogenization scheme: The FE2-method. Plasticity and Beyond. Springer, Vienna. 2014;550:1-64.
37. van den Eijnden AP, Bésuelle P, Chambon R, Collin F. A FE^2 modelling approach to hydromechanical coupling in cracking-induced localization problems. *Int J Solids Struct*. 2016;97-98:475-488.

38. Frey J, Chambon R, Dascalu C. A two-scale poromechanical model for cohesive rocks. *Acta Geotech*. 2013;8(2):107-124.
39. Marinelli F, van den Eijnden AP, Sieffert Y, Chambon R, Collin F. Modeling of granular solids with computational homogenization: comparison with Biot's theory. *Finite Elem Anal Des*. 2016;119:45-62.
40. Zalamea N, Bésuelle P, Dal Pont S, Di Donna A, Multiscale modelling of the thermo-hydromechanical behaviour of argillaceous rocks. 16th International Conference on Computational Plasticity. Fundamentals and Applications (COMPLAS), Barcelona. 2021.
41. Desrues J, Argilaga A, Caillerie D, et al. From discrete to continuum modelling of boundary value problems in geomechanics: an integrated FEM-DEM approach. *Int J Numer Anal Meth Geomech*. 2019;43(5):919-955.
42. Zhang C, Armandb G, Conil N, Laurich B. Investigation on anisotropy of mechanical properties of Callovo-Oxfordian claystone. *Eng Geol*. 2019;251:128-145.
43. Zhang C, Rothfuchs T, Su K, Hoteit N. Experimental study of the thermo-hydro-mechanical behaviour of indurated clays. *Phys Chem Earth*. 2007;32(8-14):957-965.
44. Stavropoulou E, Briffaut M, Dufour F, Camps G. Time-dependent behaviour of the Callovo-Oxfordian claystone-concrete interface. *J Rock Mech Geotech Eng*. 2020;12(1):89-101.
45. Wang L, Bornert M, Héripré E, et al. Microscale insight into the influence of humidity on the mechanical behavior of mudstones. *J Geophys Res Solid Earth*. 2015;120(5):3173-3186.
46. Zeng T, Shao JF, Xua WY. Modeling of viscoplastic deformation in geomaterials with a polycrystalline approach. *Int J Rock Mech Min Sci*. 2014;72:182-190.
47. Dascalu D, François B, Keita B. A two-scale model for subcritical damage propagation. *Int J Solids Struct*. 2010;47:493-502.
48. Pardoen B, Bésuelle P, Dal Pont S, Cosenza P, Desrues J. Accounting for small-scale heterogeneity and variability of clay rock in homogenised numerical micromechanical response and microcracking. *Rock Mech Rock Eng*. 2020;53(6):2727-2746.
49. van den Eijnden AP, Bésuelle P, Collin F, Chambon R, Desrues J. Modeling the strain localization around an underground gallery with a hydro-mechanical double scale model; effect of anisotropy. *Comput Geotech*. 2017;85:384-400.
50. Salih S, Davey K, Zou ZM. A computationally efficient cohesive zone model for fatigue. *Fatigue Fract Eng Mater Struct*. 2018;42(2):1-15.
51. van den Eijnden B. *Multi-Scale Modelling of the Hydro-Mechanical Behaviour of Argillaceuous Rocks*. PhD thesis. Universite Grenoble Alpes, Université de Liège; 2015.
52. Perzyna P. Fundamental problems in viscoplasticity. *Advances in Applied Mechanics*. Academic Press; 1966.
53. Lemaitre J, Chaboche J. *Mechanics of Solid Materials*. Cambridge University Press; 1990.
54. Cristescu N. A procedure to determine non-associated constitutive equations for geomaterials. *Int J Plast*. 1994;10(2):103-131.
55. Pellet F, Hajdu A, Deleruyelle F, Besnus F. A viscoplastic model including anisotropic damage for the time dependent behaviour of rock. *Int J Numer Anal Meth Geomech*. 2005;29:941-970.
56. Detournay E. Elastoplastic model of a deep tunnel for a rock with variable dilatancy. *Rock Mech Rock Eng*. 1986;19:99-108.
57. Simo JC, Hughes TJR. *Computational Inelasticity*. Springer; 1998.
58. Hill R. A self-consistent mechanics of composite materials. *J Mech Phys Solids*. 1965;13(4):213-222.
59. Mandel J. Plasticité classique et viscoplasticité. *CISM lecture notes*. 1972:97.
60. Mánica M, Gens A, Vaunat J, Ruiz FD. A time-dependent anisotropic model for argillaceous rocks. Application to an underground excavation in Callovo-Oxfordian claystone. *Int Comput Geotech*. 2017;85:341-350.
61. Souley M, Armand G, Su K, Ghoreychi M. Modeling the viscoplastic and damage behavior in deep argillaceous rocks. *Phys Chem Earth*. 2011;36(17-18):1949-1959.
62. Shahbodagh B, Mac TN, Esgandani GA, Khalili N. A bounding surface viscoplasticity model for time-dependent behavior of soils including primary and tertiary creep. *Int J Geomech*. 2020;20(9):04020143.
63. Doghri I, Ouaar A. Homogenization of two-phase elasto-plastic composite materials and structures: study of tangent operators, cyclic plasticity and numerical algorithms. *Int J Solids Struct*. 2003;40(7):1681-1712.
64. Lee JH, Zhang Y. On the numerical integration of a class of pressure-dependent plasticity models with mixed hardening. *Int J Numer Meth Eng*. 1991;32(2):419-438.
65. Zeng T, Shao JF, Yao Y. An upscaled model for elastoplastic behavior of the Callovo-Oxfordian argillite. *Comput Geotech*. 2019;112:81-92.
66. Zeng T, Liu ZB, Jia CJ, Yao Y. Elasto-plastic behavior of the Fontainebleau sandstone based on a refined continuous strain deviation approach. *Eur J Environ Civ Eng*. 2020;26(9):3788-3804.

How to cite this article: Sun Y, Pardoen B, van den Eijnden B, Wong H. Modelling the time-dependent mechanical behaviour of clay rocks based on meso- and micro-structural viscous properties. *Int J Numer Anal Methods Geomech*. 2023;1-32. https://doi.org/10.1002/nag.3617

APPENDIX A: THERMODYNAMIC CONSISTENCY OF THE VISCOPLASTIC MODEL

From Equation (24), the viscoplastic dissipation is defined as:

$$\Phi_{vp} = \sigma_{ij}\,\dot{\varepsilon}_{ij}^{vp} = \frac{1}{\eta}\left\langle \frac{q + \alpha^{vp} p - \sigma_s}{\sigma_r} \right\rangle^n e^{-k\,\gamma^{vp}}\,(q + \beta^{vp} p) \tag{A-1}$$

The thermodynamic consistency implies that $\Phi_{vp} \geq 0$ (i.e., the viscoplastic dissipation must be non-negative). In regard to the form of Equation (A-1), this requirement should be examined considering two cases: $\sigma_{ij} \geq 0$ (tensile stress for $i = j$) and $\sigma_{ij} < 0$ (compressive stress for $i = j$). In the first case, it can be seen that $G_{vp} = q + \beta^{vp} p \geq 0$ and thereby $\Phi_{vp} \geq 0$. In the second case, considering the overstress concept that creep deformation develops only if the stress state is outside the elastic domain, that is, $F_{vp} = q + \alpha^{vp} p - \sigma_s > 0$, the non-negativity of Φ_{vp} leads to the following requirement:

$$\alpha^{vp} \geq \beta^{vp} \tag{A-2}$$

Indeed, Equation (20) leads to $G_{vp} = q + \beta^{vp}\,p = q + \alpha^{vp}\,p + (\alpha^{vp} - \beta^{vp})(-p) > 0$ if the inequality (A-2) is fulfilled. The inequality (A-2) is realistic for geomaterials for which associated viscoplastic flow rules might predict too much creep dilatancy, and for which non-associated viscoplastic flow rules are more suitable. Its physical meaning implies that the creep dilatancy is smaller than the creep yield sensitivity to the mean stress level. It is quite similar to the observation, under elastoplastic behaviour, that the dilation angles of clays and clay rocks are generally smaller than their friction angles. Moreover, these parameters α^{vp} and β^{vp} need to be calibrated based on experimental data.

APPENDIX B: ELASTOPLASTIC STRESS UPDATE

The procedures for updating the elastoplastic stress in the clay aggregates is defined hereafter. For brevity of notation, the subscript $n + 1$ at the end of a time step is omitted to express the quantities in the new current material configuration, that is, at the actual time $t = t_{n+1}$. The implicit Euler scheme is adopted here and also for the viscoplastic stresses update in Appendix C. During a time interval $\Delta t = t_{n+1} - t_n$ from times t_n to t_{n+1}, the elastoplastic model can be described with the following incremental forms:

$$\Delta\,\underline{\underline{\sigma}} = \mathbb{C}^e : \Delta\underline{\underline{\boldsymbol{\varepsilon}}}^{\boldsymbol{e}} = \mathbb{C}^e : \left(\Delta\underline{\underline{\varepsilon}} - \Delta\underline{\underline{\boldsymbol{\varepsilon}}}^{\boldsymbol{p}}\right) \tag{B-1}$$

$$\Delta\underline{\underline{\boldsymbol{\varepsilon}}}^{\boldsymbol{p}} = \frac{1}{2}\Delta\varepsilon_p^p\,\underline{\underline{\boldsymbol{\delta}}} + \Delta\varepsilon_q^p\,\underline{\underline{\boldsymbol{n}}} \tag{B-2}$$

$$\Delta\,\gamma^p = \Delta\varepsilon_q^p \tag{B-3}$$

and the plastic function:

$$F_{ep}\,(p, q, \gamma^p) = 0 \tag{B-4}$$

In Equation (B-1), $\mathbb{C}^e$ is the Hooke elastic constitutive tangent tensor. The stress at the end of the current time step is elastically predicted:

$$\underline{\underline{\boldsymbol{\sigma}}} = \underline{\underline{\boldsymbol{\sigma}}}_n + \Delta\,\underline{\underline{\boldsymbol{\sigma}}} = \underline{\underline{\boldsymbol{\sigma}}}_n + \mathbb{C}^e : \left(\Delta\underline{\underline{\varepsilon}} - \Delta\underline{\underline{\varepsilon}}^p\right) = \underline{\underline{\boldsymbol{\sigma}}}^{tr} - K\Delta\varepsilon_p^p\,\underline{\underline{\boldsymbol{\delta}}} - 2G\Delta\varepsilon_q^p\,\underline{\underline{\boldsymbol{n}}} \tag{B-5}$$

$$\underline{\underline{\boldsymbol{\sigma}}}^{tr} = \underline{\underline{\boldsymbol{\sigma}}}_n + \mathbb{C}^e : \Delta\underline{\underline{\varepsilon}} \tag{B-6}$$

where the superscript ‘*tr*’ represents the elastic trial state. Thus, $\underline{\underline{\boldsymbol{\sigma}}}^{tr}$ is the elastic stress predictor or elastic trial stress. Moreover, the elastic parameters are G the shear modulus and K the bulk modulus of the material. From Equation (B-5), the mean stress p and the deviatoric stress q are obtained as follows:

$$p = p^{tr} - K\Delta\varepsilon_p^p \tag{B-7}$$

$$q = q^{tr} - 2G\Delta\varepsilon_q^p \tag{B-8}$$

After some algebraic operations, the following relation is obtained:

$$\underline{\underline{\boldsymbol{n}}} = \underline{\underline{\boldsymbol{n}}}^{tr} = \frac{3\,\underline{\underline{\boldsymbol{s}}}^{tr}}{2q^{tr}} \tag{B-9}$$

A residual vector $\vec{\boldsymbol{r}} = \{r_1 \;\; r_2\}^{\mathrm{T}}$ is then defined, in which r_1 and r_2 are written as follows:

$$r_1 = \Delta\varepsilon_p^p \frac{\partial G_{ep}}{\partial q} - \Delta\varepsilon_q^p \frac{\partial G_{ep}}{\partial p} \tag{B-10}$$

$$r_2 = F_{ep}\;(p, q, \gamma^p) \tag{B-11}$$

The unknows in the above two equations are $\vec{\boldsymbol{x}} = \{\Delta\varepsilon_p^p \;\; \Delta\varepsilon_q^p\}^{\mathrm{T}}$. To find a solution $\vec{\boldsymbol{x}}'$ that cancels the residuals such that $\vec{\boldsymbol{r}}(\vec{\boldsymbol{x}}') = \vec{0}$, the well-known Newton–Raphson method is used to solve the equations since it has a second order (i.e., quadratic) convergence rate. In each iteration, the corrections of the unknowns $d\Delta\varepsilon_p^p$ and $d\Delta\varepsilon_q^p$, giving the unknow correction vector $d\vec{\boldsymbol{x}} = \{d\Delta\varepsilon_p^p \;\; d\Delta\varepsilon_q^p\}^{\mathrm{T}}$, are obtained by solving:

$$\underline{\underline{\boldsymbol{A}}}\, d\vec{\boldsymbol{x}} = -d\vec{\boldsymbol{r}} \Leftrightarrow \begin{bmatrix} A_{11} & A_{12} \\ A_{21} & A_{22} \end{bmatrix} \begin{Bmatrix} d\Delta\varepsilon_p^p \\ d\Delta\varepsilon_q^p \end{Bmatrix} = -\begin{Bmatrix} dr_1 \\ dr_2 \end{Bmatrix} \tag{B-12}$$

where the four components of the Jacobian matrix A_{ij} $(i,j = 1,2)$ are defined at the end of this section. The stress at the end of the time step, that is, at time $t = t_{n+1}$, can then be updated using Equation (B-5).

The consistent tangent modulus provides a softer overall REA response, but can increase the stability of the local constitutive integration and homogenisation process.[63] Therefore, the consistent tangent operator instead of continuum tangent operator is used hereafter. The commonly used elastoplastic consistent tangent modulus is $\frac{\partial\,\underline{\underline{\sigma}}}{\partial\,\underline{\underline{\varepsilon}}}$ which is defined as the variation of stress caused by the variation of total strain at the end of the time step. However, another form of elastoplastic consistent tangent modulus is used here:

$$\mathbb{C}^{ep} = \frac{\partial\,\underline{\underline{\boldsymbol{\sigma}}}}{\partial\,\underline{\underline{\boldsymbol{\varepsilon}}}^{tr}} \tag{B-13}$$

where $\mathbb{C}^{ep}$ is defined as the variation of stress caused by the variation of elastic trial strain (i.e., elastic strain predictor):

$$\underline{\underline{\boldsymbol{\varepsilon}}}^{tr} = \underline{\underline{\boldsymbol{\varepsilon}}}^{\mathbf{e}} = \underline{\underline{\boldsymbol{\varepsilon}}} - \underline{\underline{\boldsymbol{\varepsilon}}}_n^{p} = \underline{\underline{\boldsymbol{\varepsilon}}}_n + \Delta\underline{\underline{\boldsymbol{\varepsilon}}} - \underline{\underline{\boldsymbol{\varepsilon}}}_n^{p} \tag{B-14}$$

at the end of current time step. Such scheme proposed by Lee and Zhang[64] is able to deal with certain extreme cases without extra matrix inversion, and has been successfully implemented by Zeng et al.[65,66]

Differentiating Equation (B-5) gives:

$$d\,\underline{\underline{\boldsymbol{\sigma}}} = \mathbb{C}^{ep} : d\,\underline{\underline{\boldsymbol{\varepsilon}}}^{tr} = \left(\mathbb{C}^{e} - K\underline{\underline{\boldsymbol{\delta}}} \otimes \frac{\partial\Delta\varepsilon_p^p}{\partial\,\underline{\underline{\boldsymbol{\varepsilon}}}^{tr}} - 2G\underline{\underline{\boldsymbol{n}}} \otimes \frac{\partial\Delta\varepsilon_q^p}{\partial\,\underline{\underline{\boldsymbol{\varepsilon}}}^{tr}} - 2G\Delta\varepsilon_q^p \frac{\partial\underline{\underline{\boldsymbol{n}}}^{tr}}{\partial\,\underline{\underline{\boldsymbol{\varepsilon}}}^{tr}}\right) : d\,\underline{\underline{\boldsymbol{\varepsilon}}}^{tr} \tag{B-15}$$

and differentiating Equations (B-10) and (B-11) gives:

$$\underline{\underline{\boldsymbol{A}}}\, d\vec{\boldsymbol{x}} = -d\vec{\boldsymbol{r}} = \begin{bmatrix} A_{11} & A_{12} \\ A_{21} & A_{22} \end{bmatrix} \begin{Bmatrix} d\Delta\varepsilon_p^p \\ d\Delta\varepsilon_q^p \end{Bmatrix} = -\begin{Bmatrix} b_{11}dp^{tr} + b_{12}dq^{tr} \\ b_{21}dp^{tr} + b_{22}dq^{tr} \end{Bmatrix} \tag{B-16}$$

where the values of coefficients b_{ij} $(i,j = 1,2)$ are defined in function of the expression of F_{ep} and G_{ep} (in Equation (B-21)). Solving the above equations gives the linear relationship between $d\Delta\varepsilon_p^p$, $d\Delta\varepsilon_q^p$, dp^{tr} and dq^{tr}.

$$\begin{aligned} d\Delta\varepsilon_p^p &= c_{11}\,dp^{tr} + c_{12}dq^{tr} \\ d\Delta\varepsilon_q^p &= c_{21}\,dp^{tr} + c_{22}d\,q^{tr} = q^{tr} - 2G\Delta\varepsilon_q \end{aligned} \tag{B-17}$$

where $c_{11} = \frac{A_{12}b_{21}-b_{11}A_{22}}{\det(\underline{\underline{\boldsymbol{A}}})}$; $c_{12} = \frac{A_{12}b_{22}-b_{12}A_{22}}{\det(\underline{\underline{\boldsymbol{A}}})}$; $c_{21} = \frac{A_{21}b_{11}-b_{21}A_{11}}{\det(\underline{\underline{\boldsymbol{A}}})}$; $c_{22} = \frac{A_{21}b_{12}-b_{22}A_{11}}{\det(\underline{\underline{\boldsymbol{A}}})}$; $det\,(\underline{\underline{\boldsymbol{A}}}) = A_{11}\,A_{22} - A_{12}A_{21}$.

Finally, the consistent tangent modulus $\mathbb{C}^{ep}$ writes[66]:

$$\mathbb{C}^{ep} = \mathbb{C}^{e} - c_{11}K^2\underline{\underline{\boldsymbol{\delta}}} \otimes \underline{\underline{\boldsymbol{\delta}}} - 2c_{12}KG\underline{\underline{\boldsymbol{\delta}}} \otimes \underline{\underline{\boldsymbol{n}}}^{tr} - 2c_{21}KG\underline{\underline{\boldsymbol{n}}}^{tr} \otimes \underline{\underline{\boldsymbol{\delta}}} - 4G^2c_{22}\underline{\underline{\boldsymbol{n}}}^{tr} \otimes \underline{\underline{\boldsymbol{n}}}^{tr} - \frac{4G^2\Delta\varepsilon_q^p}{q^{tr}}\left(\frac{3}{2}\mathbb{K} - \underline{\underline{\boldsymbol{n}}}^{tr} \otimes \underline{\underline{\boldsymbol{n}}}^{tr}\right) \tag{B-18}$$

where the fourth-order deviatoric identity tensor (projection tensor) $\mathbb{K}$ writes, in indicial notation, $\mathrm{K}_{ijkl} = \mathrm{I}_{ijkl} - \mathrm{J}_{ijkl}$ with the fourth-order symmetric identity tensor $\mathrm{I}_{ijkl} = \frac{1}{2}\left(\delta_{ik}\delta_{jl} + \delta_{il}\delta_{jk}\right)$ and the fourth-order volumetric (spherical) identity tensor $\mathrm{J}_{ijkl} = \frac{1}{2}\,\delta_{ij}\delta_{kl}$.

Eventually, for F_{ep} and G_{ep} given by Equations (10) and (13), and their hardening functions α^p and β^p from Equations (11) and (14), the expressions of the coefficients of A_{ij} and b_{ij} are given by:

$$\begin{aligned} A_{11} &= \frac{\partial r_1}{\partial\Delta\varepsilon_p^p} = 1; A_{12} = \frac{\partial r_1}{\partial\Delta\varepsilon_q^p} = -\beta^p\left(\varepsilon_q^p\right) + \Delta\varepsilon_q^p\frac{\partial\beta^p\left(\varepsilon_q^p\right)}{\partial\Delta\varepsilon_q^p}; \\ A_{21} &= \frac{\partial r_2}{\partial\Delta\varepsilon_p^p} = -K\alpha^p\left(\varepsilon_q^p\right); A_{22} = \frac{\partial r_2}{\partial\Delta\varepsilon_q^p} = -2G + \left(p^{tr} - K\Delta\varepsilon_p^p - c_0\right)\frac{\partial\alpha^p\left(\varepsilon_q^p\right)}{\partial\Delta\varepsilon_q^p}; \end{aligned} \tag{B-19}$$

$$\frac{\partial\alpha^p\left(\varepsilon_q^p\right)}{\partial\Delta\varepsilon_q^p} = b\left(\alpha_m^p - \alpha_0^p\right)\,e^{-b\left(\varepsilon_{q;n}^p + \Delta\varepsilon_q^p\right)}; \frac{\partial\beta^p\left(\varepsilon_q^p\right)}{\partial\Delta\varepsilon_q^p} = b'\,\left(\beta_m^p - \beta_0^p\right)\,e^{-b'\left(\varepsilon_{q;n}^p + \Delta\varepsilon_q^p\right)} \tag{B-20}$$

$$b_{11} = \frac{\partial r_1}{\partial p^{tr}} = 0; b_{12} = \frac{\partial r_1}{\partial q^{tr}} = 0; b_{21} = \frac{\partial r_2}{\partial p^{tr}} = \alpha^p\,\left(\varepsilon_q^p\right); b_{22} = \frac{\partial r_2}{\partial q^{tr}} = 1 \tag{B-21}$$

APPENDIX C: VISCOPLASTIC STRESS UPDATE

The procedures for updating the viscoplastic stress in the clay aggregates is defined hereafter. As previously, we drop the subscript $n+1$ of the variable at time t_{n+1} for brevity of notation. During a time interval $\Delta t = t_{n+1} - t_n$ from times t_n to t_{n+1}, the viscoplastic rate equations (21) and (24) are defined in incremental forms as:

$$\Delta\underline{\underline{\boldsymbol{\varepsilon}}}^{vp} = \Delta t\left[(1-\theta)\,\underline{\underline{\dot{\boldsymbol{\varepsilon}}}}_n^{vp} + \theta\,\underline{\underline{\dot{\boldsymbol{\varepsilon}}}}^{vp}\right] \tag{C-1}$$

$$\Delta\,\gamma^{vp} = \Delta t\,\left[(1-\theta)\,\dot{\gamma}_n^{vp} + \theta\dot{\gamma}^{vp}\right] \tag{C-2}$$

where θ is an integration parameter ranging from 0 to 1. $\theta = 0$ corresponds to an explicit Euler time integration scheme and $\theta = 1$ to an implicit Euler scheme.

For a viscoplastic model like Equation (24), the stress tensor and the hardening variable at time $t = t_{n+1}$ can be written as:

$$\underline{\underline{\boldsymbol{\sigma}}} = \underline{\underline{\boldsymbol{\sigma}}}^{tr} - \mathbb{C}^e : \Delta\underline{\underline{\boldsymbol{\varepsilon}}}^{vp} = \underline{\underline{\boldsymbol{\sigma}}}^{tr} - \frac{\Delta t}{\eta}\mathbb{C}^e : \left(F^n\,e^{-k\gamma^{vp}}\frac{\partial G_{vp}}{\partial\,\underline{\underline{\boldsymbol{\sigma}}}}\right) \tag{C-3}$$

$$\gamma^{vp} = \gamma_n^{vp} + \Delta\,\gamma^{vp} = \gamma_n^{vp} + \Delta t\,\dot{\gamma}^{vp} \tag{C-4}$$

where $\mathbb{C}^e$ is the fourth-order elastic stiffness tensor; $\underline{\underline{\boldsymbol{\sigma}}}^{tr} = \underline{\underline{\boldsymbol{\sigma}}}_n + \mathbb{C}^e : \Delta\underline{\underline{\boldsymbol{\varepsilon}}}$ is the elastic stress predictor at time $t = t_{n+1}$; $\langle\frac{F_{vp}}{\sigma_r}\rangle^n$ is replaced by $F^n = \langle\frac{F_{vp}}{\sigma_r}\rangle^n$ for writing simplicity. The residual equations based on Equations (C-3) and (C-4) are written as follows:

$$\underline{\underline{\boldsymbol{r}}}_1 = \underline{\underline{\boldsymbol{\sigma}}} - \underline{\underline{\boldsymbol{\sigma}}}^{tr} + \frac{\Delta t}{\eta}\mathbb{C}^e : \left(F^n\,\mathrm{e}^{-k\gamma^{vp}}\frac{\partial G_{vp}}{\partial\,\underline{\underline{\boldsymbol{\sigma}}}}\right) \tag{C-5}$$

$$r_2 = \gamma^{vp} - \gamma_n^{vp} - \frac{\Delta t}{\eta}\left(F^n\,\mathrm{e}^{-k\gamma^{vp}}\right) \tag{C-6}$$

Symbolically, Equation (C-5) is a tensor equation, but we can assume it to be vectorised so that the total residual vector may be defined as $\vec{\boldsymbol{r}} = \{\underline{\underline{\boldsymbol{r}}}_1 \quad r_2\}^{\mathrm{T}}$, where $\vec{\boldsymbol{x}} = \{\underline{\underline{\boldsymbol{\sigma}}} \ \gamma^{vp}\}^{\mathrm{T}}$ is the vectorised set of unknowns.

To find a solution $\vec{\boldsymbol{x}}$' that cancels the residuals such that $\vec{\boldsymbol{r}}\,(\vec{\boldsymbol{x}}') = \vec{0}$, the Newton–Raphson method is used to solve the equations and the following Jacobian matrix is needed in each iteration:

$$\underline{\underline{\boldsymbol{A}}} = \begin{bmatrix} \underline{\underline{\boldsymbol{A}}}_{11} & \vec{A}_{12} \\ \vec{A}_{21}^{T} & A_{22} \end{bmatrix} = \begin{bmatrix} \dfrac{\partial \underline{\underline{\boldsymbol{r}}}_1}{\partial \underline{\underline{\boldsymbol{\sigma}}}} & \dfrac{\partial \underline{\underline{\boldsymbol{r}}}_1}{\partial \gamma^{vp}} \\ \dfrac{\partial r_2}{\partial \underline{\underline{\boldsymbol{\sigma}}}} & \dfrac{\partial r_2}{\partial \gamma^{vp}} \end{bmatrix} \tag{C-7}$$

Note that $\underline{\underline{\boldsymbol{A}}}_{11}$ is a 4×4 submatrix for full 2D applications, $\vec{\mathbf{A}}_{12}$ and $\vec{\mathbf{A}}_{21}^{T}$ are column and row vectors, and A_{22} is a scalar. The elements in the matrix $\underline{\underline{\boldsymbol{A}}}$ include:

$$\underline{\underline{\boldsymbol{A}}}_{11} = \frac{\partial \underline{\underline{\boldsymbol{r}}}_1}{\partial \underline{\underline{\boldsymbol{\sigma}}}} = \mathbb{I} + \frac{\Delta t}{\eta}\mathbb{C}^e : \left[e^{-k\gamma^{vp}} \left(F^n \frac{\partial G_{vp}^2}{\partial^2 \underline{\underline{\boldsymbol{\sigma}}}} + \frac{\partial F^n}{\partial \underline{\underline{\boldsymbol{\sigma}}}} \otimes \frac{\partial G_{vp}}{\partial \underline{\underline{\boldsymbol{\sigma}}}} \right) \right] \tag{C-8}$$

$$\vec{\boldsymbol{A}}_{12} = \frac{\partial \underline{\underline{\boldsymbol{r}}}_1}{\partial \gamma^{vp}} = \frac{\Delta t}{\eta}\,\mathbb{C}^e : \left[-k\, e^{-k\gamma^{vp}} F^n \left(\frac{3\underline{\underline{\boldsymbol{s}}}}{2q} + \frac{\alpha^{vp}}{2}\underline{\underline{\boldsymbol{\delta}}} \right) \right] \tag{C-9}$$

$$\vec{\boldsymbol{A}}_{21} = \frac{\partial r_2}{\partial \underline{\underline{\boldsymbol{\sigma}}}} = \frac{\Delta t}{\eta} \left(-e^{-k\gamma^{vp}} \frac{\partial F^n}{\partial \underline{\underline{\boldsymbol{\sigma}}}} \right) \tag{C-10}$$

$$A_{22} = \frac{\partial r_2}{\partial \gamma^{vp}} = 1 + \frac{\Delta t}{\eta} \left(k\, e^{-k\gamma^{vp}} F^n \right) \tag{C-11}$$

where II is the fourth-order symmetric unit tensor writes $\mathrm{I}_{ijkl} = \frac{1}{2}\left(\delta_{ik}\delta_{jl} + \delta_{il}\delta_{jk}\right)$. The initial values of the unknows at the beginning of the iteration correspond to the converged solutions at the last time step in implicit method (or to the results calculated by the explicit method in the current time step). The update of the unknowns after the *i*-1th iteration then writes:

$$\vec{\boldsymbol{x}}^{i} = \vec{\boldsymbol{x}}^{i-1} - \left(\underline{\underline{\boldsymbol{A}}}^{i-1} \right)^{-1} \vec{\boldsymbol{x}}^{i-1} \tag{C-12}$$

According to the chain rule, the updated algorithm viscoplastic tangent modulus $\mathbb{C}^{vp}$ at time t_{n+1} is calculated by:

$$\mathbb{C}^{vp} = \left(\underline{\underline{\boldsymbol{A}}}'_{11} \right)^{-1} : \mathbb{C}^e \tag{C-13}$$

where $\underline{\underline{\boldsymbol{A}}}'_{11}$ is the value of $\underline{\underline{\boldsymbol{A}}}_{11}$ evaluated at the converged local configuration $\vec{\boldsymbol{x}}$'.